

A 2700-year annual timescale and accumulation history for an ice core from Roosevelt Island, West Antarctica

Mai Winstrup^{1,*}, Paul Vallelonga¹, Helle A. Kjær¹, Tyler J. Fudge², James E. Lee³, Marie H. Riis¹, Ross Edwards^{4,5}, Nancy A.N. Bertler^{6,7}, Thomas Blunier¹, Ed J. Brook³, Christo Buizert³, Gabriela Ciobanu¹, Howard Conway², Dorte Dahl-Jensen¹, Aja Ellis⁴, B. Daniel Emanuelsson^{6,7}, Richard C.A. Hindmarsh⁸, Elizabeth D. Keller⁷, Andrei V. Kurbatov⁹, Paul A. Mayewski⁹, Peter D. Neff¹⁰, Rebecca L. Pyne⁷, Marius F. Simonsen¹, Anders Svensson¹, Andrea Tuohy^{6,7}, Edwin D. Waddington², Sarah Wheatley⁹

1: Centre for Ice and Climate, Niels Bohr Institute, University of Copenhagen, Copenhagen, Denmark

2: Earth and Space Sciences, University of Washington, Seattle, WA, USA

3: College of Earth, Ocean, and Atmospheric Sciences, Oregon State University, Corvallis, OR, USA

4: Physics and Astronomy, Curtin University, Perth, Western Australia, Australia

5: Department of Civil and Environmental Engineering, University of Wisconsin-Madison, Madison, USA

6: Antarctic Research Centre, Victoria University of Wellington, Wellington, New Zealand

7: GNS Science, Lower Hutt, New Zealand

8: British Antarctic Survey, Cambridge, UK

9: Climate Change Institute, University of Maine, Orono, Maine, USA

10: Earth and Environmental Sciences, University of Rochester, Rochester, NY, USA

*: Now at: Danish Meteorological Institute, Copenhagen, Denmark

Correspondance to: Mai Winstrup (mai@nbi.ku.dk)

Abstract

We present a 2700-year annually-resolved chronology and snow accumulation history for the Roosevelt Island Climate Evolution (RICE) ice core, Ross Ice Shelf, West Antarctica. The core adds information on past accumulation changes in an otherwise poorly constrained sector of Antarctica.

The timescale was constructed by identifying annual cycles in high-resolution impurity records, and it constitutes the top part of the Roosevelt Island Ice Core Chronology 2017 (RICE17). Validation by volcanic and methane matching to the WD2014 chronology from the WAIS Divide ice core shows that the two timescales are in excellent agreement. In a companion paper, gas matching to WAIS Divide is used to extend the timescale for the deeper part of the core where annual layers cannot be identified.

Based on the annually-resolved timescale, we produced a record of past snow accumulation at Roosevelt Island. The accumulation history shows that Roosevelt Island experienced slightly increasing accumulation rates between 700 BCE and 1300 CE, with an average accumulation of 0.25 ± 0.02 m water equivalent (w.e.) per year. Since 1300 CE, trends in the accumulation rate have been consistently negative, with an acceleration in the rate of decline after the mid-17th century. The current accumulation rate at Roosevelt Island is 0.210 ± 0.002 m w.e. y^{-1} (average since 1965 CE, $\pm 2\sigma$), and rapidly declining with a trend corresponding to 0.8 mm yr^{-1}

42 ². The decline observed since the mid-1960s is 8 times faster than the long-term decreasing
43 trend taking place over the previous centuries, with decadal mean accumulation rates
44 consistently being below average.

45 Previous research has shown a strong link between Roosevelt Island accumulation rates and the
46 location and intensity of the Amundsen Sea Low (ASL), with significant impact on regional
47 sea ice extent. The decrease in accumulation rates at Roosevelt Island may therefore be
48 explained in terms of a recent strengthening of the ASL and expansion of sea ice in the Eastern
49 Ross Sea. The start of the rapid decrease in RICE accumulation rates observed in 1965 CE may
50 thus mark the onset of significant increases in regional sea ice extent.

51 **1. Introduction**

52 Accurate timescales are fundamental for reliable interpretation of paleoclimate archives,
53 including ice cores. Ice-core chronologies can be produced in a variety of ways. Where annual
54 snow deposition is sufficiently high and reasonably regular throughout the year, seasonal
55 variations in site temperature and atmospheric impurity deposition lead to annual cycles in the
56 ice-core water isotope and impurity records (Dansgaard, 1964; Hammer et al., 1978). By
57 identifying and counting the annual cycles, an annual-layer-counted ice-core timescale can be
58 produced (Sigl et al., 2016; Steig et al., 2005; Svensson et al., 2008). This technique is
59 commonly employed for producing ice-core timescales at sites with moderate to high snow
60 accumulation, including coastal Antarctica. Annual-layer-counted ice-core timescales have
61 traditionally been obtained by manual counting, but this task can now be performed using
62 machine-learning algorithms for pattern recognition (Winstrup et al., 2012).

63 Where possible, identification of annual layers allows the development of a high-resolution ice-
64 core chronology, but unless constrained by other data, the uncertainty of such a timescale will
65 increase with depth, as the number of uncertain layers accumulate to produce some age
66 uncertainty (Andersen et al., 2006; Rasmussen et al., 2006). Marker horizons found in the ice-
67 core records can be used to evaluate the accuracy of a layer-counted timescale, or, alternatively,
68 to constrain the timescale. Such marker horizons carry evidence of events of global or regional
69 nature, and may be; (a) layers of enhanced radioactivity resulting from nuclear bomb tests
70 (Arienzo et al., 2016); (b) sulfuric acids (Hammer, 1980) and/or tephra (Abbott et al., 2012)
71 from volcanic eruptions; or (c) enhanced flux of cosmogenic radionuclides caused by changes
72 in solar activity, reduction of the Earth's magnetic field, or cosmic events (Muscheler et al.,
73 2014; Raisbeck et al., 2017; Sigl et al., 2015).

74 Ice cores can also be stratigraphically matched using records of past atmospheric composition
75 from trapped air in the ice (Blunier, 2001; Blunier et al., 1998; EPICA Community Members,
76 2006). Variations in atmospheric composition are globally synchronous. Accounting for the
77 time required to sequester the air into the ice, the ice-core gas records can be used also for
78 stratigraphic matching of records measured on the ice matrix. Even during periods of stable
79 climate, the atmospheric composition displays multi-decadal fluctuations (Bender et al., 1994;
80 Mitchell et al., 2011, 2013) allowing synchronization on sub-centennial timescales.

81 Annually-resolved ice-core chronologies provide long-term reconstructions of annual snow
82 accumulation (Alley et al., 1993; Dahl-Jensen et al., 1993): Annual layer thicknesses can be
83 converted to past accumulation rates by applying corrections due to density changes during the
84 transformation from snow to ice (Herron and Langway, 1980), and thinning of annual layers
85 caused by ice flow (Nye, 1963). Reconstructions of past accumulation rates are important for
86 improving our understanding of the natural fluctuations in snow accumulation and their climate
87 drivers. Such knowledge is essential to accurately evaluate the current and future surface mass

88 balance of glaciers and ice sheets, a critical and currently under-constrained factor in sea level
89 assessments (Shepherd et al., 2012).

90 Here we present an ice-core chronology (RICE17) and accumulation history for the last 2,700
91 years from Roosevelt Island, an ice rise located in the Eastern Ross Embayment, Antarctica
92 (Fig. 1). The ice core was extracted as part of the Roosevelt Island Climate Evolution (RICE)
93 project (2010-2014) (Bertler et al., 2018). RICE forms a contribution to the Antarctica2k
94 network (Stenni et al., 2017; Thomas et al., 2017), which seeks to produce Antarctica-wide ice-
95 core reconstructions of temperature and snow accumulation for the past 2000 years. The
96 chronology presented here was produced by annual-layer counting. In a companion paper (Lee
97 et al., 2018), we extend the timescale to cover the deeper core by gas matching to the WAIS
98 Divide ice core on the WD2014 chronology (Buizert et al., 2015; Sigl et al., 2016).

99 ECMWF ERA-Interim (ERAi) reanalysis fields (Dee et al., 2011) indicate that precipitation at
100 Roosevelt Island is strongly influenced by the Amundsen Sea Low (ASL) and associated
101 ridging (Raphael et al., 2016), and anti-correlated with precipitation in Ellsworth Land and the
102 Antarctic Peninsula (Bertler et al., 2018; Emanuelsson et al., 2018; Hosking et al., 2013). These
103 differences emphasize the need for high spatial and temporal coverage when reconstructing
104 regional mass balance patterns. With few other ice cores from the Ross Sea region, the RICE
105 accumulation history adds information on past changes in mass balance from an otherwise
106 poorly-constrained sector of the Antarctic continent.

107 **2. Site characteristics**

108 Roosevelt Island is located within the eastern part of the Ross Ice Shelf (Fig. 1), from which it
109 protrudes as an independent ice dome that is grounded 214 meters below sea level. Snow
110 accumulates locally on the ice dome, with ice originating from the Siple Coast ice streams
111 flowing around the island in the Ross Ice Shelf. Geophysical and glaciological surveys across
112 Roosevelt Island in the 1960s established ice thickness, surface topography, surface velocity
113 and accumulation rate (Bentley and Giovinetto, 1962; Clapp, 1965; Jiracek, 1967). The island
114 was revisited during 1974-75 as part of the Ross Ice Shelf Project. During this project, shallow
115 cores (up to 70m) were collected across the ice shelf, including two firn cores from Roosevelt
116 Island summit (Clausen et al., 1979). The shortest (11 m) firn core from near the summit was
117 measured for water isotopes and total β -activity in high resolution; we here refer to it as RID-
118 75 (Table 1). Results from the shallow cores show that seasonal signals of stable isotopes and
119 ionic chemistry are well preserved in the ice (Clausen et al., 1979; Herron and Langway, 1979;
120 Langway et al., 1974).

121 Ice-penetrating radar surveys of Roosevelt Island that took place in 1997 revealed a smoothly
122 varying internal stratigraphy of isochronal reflectors (Conway et al., 1999). There was no
123 evidence of disturbed internal layering that would indicate high strain rates or buried crevasses,
124 suggesting the summit of the island to be a good place for an ice core. Of special interest was a
125 distinctive arching pattern of the internal layers beneath the divide. This pattern has implications
126 for the ice history, since isochronal layers arch upward beneath divides that are stable and frozen
127 at the bed (Raymond, 1983). Analyses of the geometry of the internal layering indicate that the
128 current divide-type ice-flow regime started about 3000 years ago (Conway et al., 1999; Martín
129 et al., 2006), and thus has been in existence throughout the time period investigated in this
130 paper. Combined with recently-measured vertical ice velocity profiles across the ice divide
131 (Kingslake et al., 2014), the stability of the ice flow regime at Roosevelt Island facilitates
132 interpretation of past accumulation rates from annual layers in the RICE ice core.

133 The RICE deep ice core was drilled at the summit of Roosevelt Island (79.364S, 161.706W,
134 550 m above sea level (Bertler et al., 2018)), and less than 1 km from the old RID-75 shallow
135 core. It was drilled in austral summers of 2011/12 and 2012/13. During the first season, the core
136 was dry-drilled down to 130 m, and then the borehole was cased. An Estisol-240/Coasol drilling
137 fluid mixture was used to maintain core quality during the second drilling season. The ice
138 thickness is 764.6 m. The upper 344 m of the core spans the past 2700 years; the period for
139 which an annual-layer-counted timescale can be constructed. In addition to the deep core,
140 several shallow cores were drilled in the vicinity. During the 2012/13 field season, a 20 m firn
141 core (RICE-12/13-B) was drilled near the main core, and it was used to extend the records up
142 to the 2012/13 snow surface. Table 1 provides an overview of the relevant firn and ice cores
143 collected at Roosevelt Island. An automated weather station near the RICE drill site recorded
144 mean annual temperatures of -23.5°C over the duration of the RICE project (2010-2014), and
145 an average snow accumulation of approximately 0.20 m w.e. yr⁻¹ (Bertler et al., 2018).

146 **Methods**

147 **3. Ice core processing and impurity analysis**

148 The RICE ice cores were processed and analyzed at the GNS Science National Ice Core Facility
149 in Lower Hutt, New Zealand. The cores were cut longitudinally to produce a 15x35 mm
150 triangular piece for water isotope analysis and two 35x35 mm square sticks for continuous flow
151 analysis (CFA) (Fig. 2). The second CFA piece was for use in case the core quality of the
152 primary piece was compromised, or for repeat measurements to test measurement accuracy and
153 system stability.

154 In parallel with ice core cutting and processing, CFA and electrical conductivity measurements
155 (ECM; Hammer (1980)) were carried out. ECM was measured using a low-power hand-held
156 instrument from Icefield Instruments Inc. directly on the ice-core surfaces after the initial
157 cutting of the core. In 2012, the uppermost section (8.57-40 m) of the RICE main core was
158 processed and analyzed using the GNS Science melter system, with continuous measurements
159 of stable water isotopes (δD , $\delta^{18}O$) and black carbon, and discrete sampling of major ion and
160 trace element concentrations. The following year, this set-up was replaced by an expanded
161 version of the Copenhagen CFA system (Bigler et al., 2011), providing high-resolution
162 continuous measurements of liquid conductivity, calcium (Ca^{2+}), insoluble dust particles,
163 acidity (H^+), and black carbon (BC), as well as stable water isotopes (δD , $\delta^{18}O$) and methane
164 gas concentrations (Table 1). The RICE-12/13-B firn core was analyzed using this system.
165 Next, the RICE main core was melted and analyzed from 40 m to 475 m, at which depth the ice
166 brittle zone was reached. Subsequent repeat measurements of the top section (8.57-40 m) of the
167 main core were made using the second, parallel CFA stick.

168 Primary adaptations to the Copenhagen CFA system involved: 1) Depth assignment via a digital
169 encoder using a 1-second sampling rate (Keller et al., 2018); 2) Continuous analysis of stable
170 water isotopes ($\delta^{18}O$, δD) using a Los Gatos Research (LGR) analyzer (Emanuelsson et al.,
171 2015); 3) Black carbon analysis by a Single Particle Soot Photometer (Droplet Measurement
172 Technologies, Boulder, CO; DMT SP2) following the method reported by McConnell et al.
173 (2007); 4) Acidity measurements based on direct registration of H^+ concentrations using an
174 optical dye method (Kjær et al., 2016); 5) Continuous methane concentration analysis using a
175 Picarro Cavity Ring-Down Spectroscopy (CRDS) instrument (Stowasser et al., 2012); and 6)
176 Inclusion of three fraction collectors for discrete sample analyses by, respectively, ion
177 chromatography (IC), Inductively-Coupled Plasma Mass Spectrometry (ICP-MS), including

178 measurements of ^{239}Pu using an ICP-SFMS technique (Gabrieli et al., 2011), and measurements
179 of stable water isotopes on the LGR. Figure 3 shows a diagram of the CFA system set-up.

180 The ice was melted at a rate of 3 cm min^{-1} , producing approximately 16.8 mL contamination-
181 free water and gas mixture per minute of melting. Air bubbles were separated in a debubbler,
182 dried, and sent to the Picarro CRDS instrument for methane analysis. Each minute, 5 mL
183 meltwater was directed to each of two fraction collectors (IC and ICP-MS aliquots) and 1.1 mL
184 was used for continuous measurements of water isotopes (0.05 mL) and black carbon (1.05 mL)
185 by the LGR and DMT SP2 instruments. The remaining 1.8 mL was sent to flow-through liquid
186 conductivity and insoluble particle analyzers (Bigler et al., 2011), and then split for continuous
187 analysis of soluble calcium (Traversi et al., 2007) and acidity (Kjær et al., 2016). A third
188 fraction collector was used to collect discrete samples for water isotopes from the melt-head
189 overflow lines originating from the outer core section, these being used for quality assurance
190 of the continuous measurements.

191 On average, 20 metres of ice were melted during a 24-hour period, including measurements,
192 calibrations and routine maintenance. Calibrations for water isotopes, calcium, acidity and
193 black carbon were carried out before and after each melting run, which comprised the
194 continuous analysis of $3\times 1\text{ m}$ long ice rods. Calibrations for methane, based on standard gases
195 with methane concentrations corresponding to glacial and preindustrial Holocene levels, were
196 carried out twice daily. Core breaks and/or contamination in the system caused some sections
197 of missing data. The percentage of affected core varied between chemistry species, ranging
198 from $<1\%$ (BC) to 17% (H^+) (see supplementary Table S1), the majority being small sections
199 of missing data that did not severely impact annual layer interpretation.

200 The CFA chemistry records were very densely sampled (1 data point per mm). Mixing in the
201 tubing as the meltwater sample travelled from melt head to the analytical systems caused
202 individual measurements to be correlated, and hence the effective depth resolution of the system
203 was significantly less than the sampling resolution. This was particularly important for the
204 RICE CFA set-up owing to the relatively small fraction of total meltwater directed to the
205 continuous measurement systems. Following the technique used in Bigler et al. (2011), the
206 effective depth resolution for the CFA measurements was estimated to range from 0.8 cm
207 (conductivity) to 2.5 cm (Ca^{2+}) (Table S1).

208 **4. Constructing the Roosevelt Island Ice Core Chronology,** 209 **RICE17, for the last 2700 years**

210 The Roosevelt Island Ice Core Chronology 2017, RICE17, was constructed using multiple
211 approaches, as necessitated by changing properties and availability of data with depth. Here we
212 describe the methodology used to construct the most recent 2700 years of RICE17, the period
213 for which annual layer identification was feasible. For the deeper part of the core, RICE17 was
214 constructed by gas matching to the WAIS Divide ice core on the WD2014 chronology, as
215 reported in Lee et al. (2018).

216 **4.1. Overview of the annual-layer counting strategy**

217 The uppermost section (0-42.34 m) of the core was dated by manual identification of annual
218 cycles in records of water isotopes and chemical impurities from the RICE main core as well
219 as the RICE-12/13-B shallow core. For this most recent period, several distinct marker horizons
220 from well-known historical events were used to constrain the chronology (section 4.2).

221 Below 42.34m (1885 CE), the timescale was augmented using the *StratiCounter* layer-counting
222 algorithm (Winstrup, 2016; Winstrup et al., 2012) applied to multiple CFA impurity records
223 from the RICE main core (section 4.3). A previously-dated tephra layer at 165 m (Pleiades;
224 1251.6±2 CE according to WD2014) was used to optimize the algorithm settings, but other than
225 that, RICE17 is a fully independent layer-counted ice-core chronology.

226 The layer-counted part of RICE17 stops at 343.72 m (700 BCE). At this depth, the annual layers
227 became too thin (<6 cm, i.e. less than 8 independent data points/year in the best resolved
228 records) for reliable layer identification in data produced by the RICE CFA set-up. The
229 timescale was extended back to 83,000 years before present using the gas-derived timescale,
230 which covers the entire core with lower resolution (Lee et al., 2018). Excellent agreement (±3
231 years) between the layer-counted timescale and the independent gas-derived age at 343.7m
232 allows us to produce the combined Roosevelt Island Ice Core Chronology 2017, RICE17, by
233 joining the two without any further adjustments.

234 **4.2. Manual layer interpretation with historical constraints (0 - 42.34 m;** 235 **2012 - 1885 CE)**

236 The top 42.34 m of the RICE17 chronology was obtained by manually counting annual layers
237 in the combined set of discretely-measured IC and ICP-MS data, where available, as well as the
238 continuous water isotope and chemistry records produced by the RICE CFA system. The RICE
239 main core starts at 8.65 m depth, so the top part of the timescale is based exclusively on the
240 RICE-12/13-B shallow core. At 12.5 m, both cores display a distinct peak in their isotope
241 profiles, showing that they can be spliced directly without need for any depth adjustments.
242 Layer marks for the top 12.5 m were placed according to the RICE-12/13-B shallow core; lower
243 layer marks refer to the main core. In the overlap section (8.65-19.55m), we used the combined
244 data set from both cores to reduce the risk of timescale errors caused by core breaks or bad data
245 sections.

246 Layer identification in this section of the core relied predominantly on annual signals in non-
247 sea-salt sulfate (nss-SO₄²⁻), acidity (H⁺) and iodine (I), as these records displayed the most
248 consistent annual signals (Fig. 4). Extreme sea-salt influx events occasionally caused large
249 sulfate peaks, necessitating the removal of the sea-salt sulfate fraction before layer
250 identification. For the top 20 m, the water isotope records also significantly strengthened the
251 annual layer interpretations. Smoothing through diffusion of water molecules in the firn,
252 however, caused the annual signal in the water isotope records to diminish with depth, resulting
253 in a loss of annual signals below 20 m.

254 Summers could be identified as periods with high stable water isotope ratios, high
255 concentrations of nss-SO₄²⁻ and associated acidity [originating from phytoplankton activity in
256 the surrounding ocean during summer (Legrand et al., 1991; Udisti et al., 1998)], and low iodine
257 concentrations [due to summertime photolysis of iodine in the snowpack (Frieß et al., 2010;
258 Spolaor et al., 2014)]. Layer marks were placed according to the depths of concurrent summer
259 peaks in water isotope ratios, nss-SO₄²⁻ concentrations, and acidity levels, and assigned a
260 nominal date of January 1st.

261 The uppermost 42.34 m of the RICE17 chronology was tied to several distinctly identifiable
262 marker horizons found in the ice-core records relating to well-known historical events (sections
263 4.2.1-4.2.3; Table 2). The timescale was obtained by identifying the most likely set of annual
264 layers, while accounting for age constraints from marker horizons (Fig. 4). We conservatively
265 estimated the age uncertainty of the marker horizons to be ±1 year, thereby allowing for some
266 uncertainty in timing of deposition of e.g. volcanic material. We further kept track of uncertain
267 layers (i.e. layers that possibly could be added or removed from the most likely set of layers,

268 while still adhering to the age constraints), thereby producing an uncertainty estimate for the
269 timescale. We interpret it as the 95% confidence interval of the age at a given depth, similar to
270 that obtained from automated layer identification deeper in the core (section 4.3).

271 **4.2.1. The 1974/75 snow surface**

272 The uppermost age constraint was established by successfully matching the RICE water isotope
273 profile to that from the RID-75 firn core (Fig. 5). Drilled in austral summer 1974/75, the snow
274 surface in RID-75 provided the first tie-point for the RICE17 chronology at a depth of 14.62m
275 (Table 2).

276 **4.2.2. Nuclear bomb peaks**

277 High-resolution ^{239}Pu measurements on the upper part of the RICE core show a significant rise
278 in plutonium levels, starting from very low background levels at 22m and reaching peak values
279 at 21.6m. This increase can be attributed to atmospheric nuclear bomb testing during the Castle
280 Bravo Operation, Marshall Islands, in March 1954, which globally caused large amounts of
281 nuclear fallout over the following year (e.g. Arienzo et al., 2016).

282 Total specific β -activity levels in the RID-75 core show the same evolution (Clausen et al.,
283 1979), confirming both the isotopic matching between the two cores, and the age attribution of
284 this event (Fig. 5). The abrupt increase in ^{239}Pu -fallout at 22m was used as age constraint for
285 the RICE17 chronology (Table 2). Subsequent peaks in the ^{239}Pu and β -activity records can be
286 attributed to successive nuclear tests and subsequent test ban treaties. These changes were much
287 less distinct, and were not used during development of the timescale.

288 **4.2.3. Recent volcanic eruptions**

289 A couple of volcanic horizons in RICE during this most recent part could be related to well-
290 known volcanic eruptions. Rhyolitic tephra located between 18.1-18.2m was found to have
291 similar geochemical composition to a tephra layer found in the WAIS Divide core deposited
292 late 1964 CE (Wheatley and Kurbatov, 2017). The tephra likely originates from Raoul Island,
293 New Zealand, which erupted from November 1964 to April 1965. This is consistent with the
294 RICE17 chronology, according to which the tephra is located in early 1965 CE (Table 2).

295 Only two volcanic eruptions could be unambiguously identified in the acidity records over this
296 period; the historical eruptions of Santa Maria (1902 CE; 37.45m) and Krakatau (1883 CE;
297 42.34m) (Table 2). These two horizons were used to constrain the deeper part of the manually-
298 counted interval of RICE17, which terminates at the Krakatau acidity peak. Deposition age of
299 volcanic material for these events was assumed identical to those observed in the WAIS Divide
300 ice core (Sigl et al., 2013). Imprints from other large volcanic eruptions taking place during
301 recent historical time, such as Agung and Pinatubo, did not manifest themselves sufficiently in
302 the RICE records to be confidently identified.

303 **4.3. Automated annual layer identification (42.34 - 343.7 m; 1885 CE -** 304 **700 BCE)**

305 For the section 42.34-343.7 m (1885 CE - 700 BCE), the RICE17 annual layer-counted
306 timescale was produced using the StratiCounter algorithm (Winstrup et al., 2012), extended to
307 interpret the annual signal based on multiple chemistry series in parallel (Winstrup, 2016).

308 StratiCounter is a Bayesian algorithm built on machine-learning methods for pattern
309 recognition, using a Hidden Markov Model (HMM) framework (Rabiner, 1989; Yu, 2010).
310 StratiCounter computes the most likely timescale and the associated uncertainty by identifying
311 annual layers in overlapping data batches stepwise down the ice core. For each batch, the
312 layering is inferred by combining prior information on layer appearance with the observed data,

313 thereby obtaining a posteriori probability distributions for the age at a given depth. The output
314 of StratiCounter is the most likely annual timescale, along with a 95% confidence interval for
315 the age as function of depth. The confidence interval assumes the timescale errors to be
316 unbiased, implying that uncertainties in layer identification partly cancel out over longer
317 distances. Previous research has documented the skill of StratiCounter to produce accurate and
318 unbiased layer-counted ice-core timescales (e.g. Sigl et al., 2015; Winstrup, 2016).

319 StratiCounter was applied to the full suite of CFA records: black carbon, acidity, insoluble dust
320 particles (42.3-129m), calcium, and conductivity. See Supplement S2 for the specifics of the
321 algorithm set-up. Figure 6 shows three depth sections of CFA data and resulting layer counts.
322 Annual cycles in the high-resolution black carbon (BC) record became more distinct prior to
323 1900 CE, and it was one of the most reliable annual proxies in the core. As observed in the
324 topmost part of the core, acidity also displayed an annual signal, although the lower effective
325 depth resolution of the acidity record (Table S1) made it less useful with depth. The calcium
326 and conductivity records frequently displayed multiple peaks per year, but contained
327 complementary information to the other proxies, and hence were also useful for layer
328 identification (Fig. 6). From 0 to 129 m, an irregular annual signal was also observed in the
329 insoluble particle record, but data below 129 m was corrupted by the presence of drill fluid in
330 the CFA system, which forced us to exclude the deeper part of this record. The discretely-
331 sampled ICP-MS data records did not have sufficient resolution to resolve annual layers.

332 Decreasing layer thicknesses caused the annual signal in the impurity records to become
333 increasingly difficult to identify with depth, and the layer-counted timescale stops at 343m (700
334 BCE).

335 **5. Reconstructing past accumulation rates**

336 The accumulation rate history at Roosevelt Island can be inferred from depth profiles of annual-
337 layer thicknesses in the RICE core, when corrected for firn densification and thinning of layers
338 due to ice flow.

339 **5.1. Changes in density with depth**

340 Bag-mean densities were measured on the main RICE core for the interval 8-130 m, at which
341 depth ice densities were reached (see Supplement S3). A steady-state Herron-Langway density
342 model (Herron and Langway, 1980) was used to extend the density profile to the surface. Using
343 observed values for initial snow density (410 kg m^{-3}), surface temperature (-23.5°C), and
344 accumulation rate ($0.22 \text{ m w.e yr}^{-1}$), the modelled density profile fits well the observed values,
345 especially for the top 50m (Fig. S1). At 8 m depth, the model agrees with the measured values,
346 providing a smooth transition between observed and modelled densities.

347 **5.2. Thinning of annual layers due to ice flow**

348 To obtain past accumulation rates, the annual layer thickness profile must be corrected for the
349 cumulative effects of ice flow on the thickness of an ice layer since it was deposited at the
350 surface (this being the ice equivalent accumulation rate at that time). The observed layer
351 thickness relative to its initial thickness as a function of depth, i.e. the “thinning function”,
352 depends on the history of vertical strain at the core site. The vertical strain rates can vary
353 significantly over short distances near ice divides, with near-surface ice flow being more
354 compressive at the divide than at the flanks (Raymond, 1983). As a result, the divide flow
355 causes an upward arch in the internal layers beneath stable ice divides. This is termed a
356 Raymond Arch, and one is present beneath the Roosevelt Island ice divide (Fig. 7c; Conway et
357 al., 1999). The vertical strain pattern was measured across Roosevelt Island (Kingslake et al.,

2014) using repeat measurements of phase sensitive radar (pRES). These measurements show significant spatial variation in the vertical velocity pattern and provide important constraints for developing the RICE thinning function.

The RICE ice core was drilled at the topographic summit of Roosevelt Island. The shallowest layers in the Raymond Arch peak below the current summit, but by mid-depth, the maximum bump amplitude of the arches is offset by approximately 500 m towards east (Figure 7c). Following Nereson and Waddington (2002), we interpret this slant in Raymond Arch position as a slight migration of the Roosevelt Island ice divide during recent centuries, with the divide previously being located 500 m east of its present position. The ice core intersects the Raymond Arch at mid-depths (~120 m; ~1500 CE) at about 70% of the maximum arch amplitude. Thus it has experienced a transitional flow regime, i.e. a mixture between pure divide flow and flank flow, for much of the past 2700 years. We consider a recent migration of the ice divide towards its present position to be the most likely scenario, with ice flow at the core site becoming increasingly divide-like over recent centuries. For this scenario, we prescribe the following history of divide migration history: Prior to 500 years before 2013 CE, the divide was located 500 m east of its present position. Since then, the divide migrated westward, arriving at its present position 250 years ago. During the migration period, the ice flow regime linearly transitioned to full divide flow, and subsequently remained as full divide flow until present. An alternative, although less likely, scenario is that the location of maximum divide-flow has always been offset from the topographic summit, in which case the ice in the core has experienced transitional flow throughout the entire period. The uncertainty on the thinning function associated with the divide history is explained in detail in the supplement (S4).

We used a one-dimensional transient ice-flow model with annual time steps to integrate the vertical strain experienced by an ice layer, and thereby track the cumulative layer thinning as function of time and depth. At each time step, the full-depth vertical velocity profile was found by scaling the shape of the vertical profile (as discussed below) with the surface velocity: The vertical surface velocity was determined as the sum of the time-varying accumulation rate and the rate of change in ice-sheet thickness. The ice-sheet thickness change was prescribed, and assumed constant in time. Model iterations were run to get an accumulation history consistent with the cumulative thinning computed by the model.

The shape of the vertical velocity profile was found by fitting an ice-flow parameterization (Liboutry, 1979) to the measured englacial velocities (Kingslake et al., 2014) corresponding to divide flow and flank flow, respectively (Fig. 7a). Details are given in the Supplementary S4. The present vertical velocity profile was constrained to match within uncertainty the current vertical velocity at the surface. During the period of transitional flow, the shape of the vertical velocity profile was taken as a linear combination of the velocity profiles for divide and flank flow, following Nereson and Waddington (2002). We used the relative amplitude of the Raymond Arch as indicator for the importance of the two flow regimes, and during the early period of transitional flow, the vertical velocity profile was weighted as 70% divide-type and 30% flank-type flow.

Figure 7b shows the resulting thinning function derived for the RICE core site. It decreases from 1.0 at the surface (no strain thinning) to 0.24 at 344 m depth. Past annual accumulation rates in water equivalents can be calculated as the annual layer thicknesses divided by the thinning function and multiplied with the firn/ice density.

5.3. Uncertainties in the accumulation history

Uncertainties in the inferred accumulation history originate from three sources: (i) identification of the annual layers; (ii) the density profile; (iii) the derived thinning function. Since the

405 RICE17 timescale was found to have negligible bias (Section 7), average layer thicknesses are
406 also not biased, and uncertainties in accumulation history due to layer identification are minor.
407 Uncertainty associated with the density correction is also small. Hence, except for the
408 uppermost part of the record (with essentially no strain thinning), uncertainty in the thinning
409 function dominates the total uncertainty, and only this factor will be considered here.

410 At the surface, uncertainty in the thinning function is zero. Increasing uncertainty with depth
411 (Fig. 7b; grey area) arises from: (a) a lack of measurements in the upper 90 m of the ice sheet
412 to constrain the present near-surface vertical velocity; (b) variation of the vertical velocity
413 profile over time as the divide may have migrated; and (c) the amount of ice-sheet thickness
414 change that has occurred. Some of the uncertainty is mitigated by the information contained in
415 the internal layering of the Roosevelt Island ice dome. The amplitudes of the Raymond stack
416 indicate that the onset of divide flow was approximately 3000 years ago (Conway et al., 1999;
417 Martín et al., 2006), i.e. prior to the period considered here; that there has been only modest
418 ice-sheet thinning; and that flow conditions have been relatively stable.

419 We develop an estimate for the uncertainty by calculating the thinning function using an
420 ensemble of model assumptions: two different parametrizations of the vertical velocity profiles,
421 two assumptions about the divide migration history, and three values of ice-sheet thickness
422 change. See Supplement S4 for an extended discussion. The uncertainty was defined as the full
423 range of these 12 scenarios, which we suggest to be a 95% confidence interval. The uncertainty
424 on the thinning function is substantial for the older portion of the record as the layers have
425 thinned to a quarter of their initial thickness.

426 **Results**

427 **6. Seasonality of impurity influx to Roosevelt Island**

428 Using the RICE17 timescale, we can quantify the seasonality of impurity influx to Roosevelt
429 Island visible in the RICE CFA records. Figure 8 shows the average seasonal pattern of the
430 various impurities at different depths, assuming constant snowfall through the year.

431 **6.1. Acidity**

432 The CFA acidity record is driven primarily by the influx of non-sea-salt sulfur-containing
433 compounds, as evident by its high resemblance to the IC non-sea-salt sulfate and ICP-MS non-
434 sea-salt sulfur records in the top part of the core (Fig. 4). Sulfur-containing compounds have a
435 variety of sources, one of which is dimethylsulfide (DMS) emissions by phytoplankton activity
436 during summer (Legrand et al., 1991; Udisti et al., 1998). Correspondingly, acidity displays a
437 regular summer signal, with maximum values in late austral summer (January/February), and
438 minimum values from June through October. This is similar in timing to the seasonal pattern of
439 non-sea-salt sulfate at Law Dome (Curran et al., 1998) and WAIS Divide (Sigl et al., 2016).
440 The acidity contains an annual signal even in the deepest part of the layer-counted timescale
441 (Fig. 8a-c).

442 **6.2. Sea-salt derived species: Calcium and conductivity**

443 As previously noted by Kjær et al. (2016), the RICE conductivity record is almost identical to
444 the mostly sea-salt-derived calcium record (see e.g. Fig. 6), suggesting sea spray to be
445 responsible also for peaks in liquid conductivity. We hence consider these two records to be
446 representative of sea salt deposition at Roosevelt Island.

447 Both records typically peak during early-to-mid-winter (June/July), but with large spread in
448 magnitude and timing from year to year (Fig. 8d-i), and oftentimes there are multiple peaks per
449 year. The timing of peak values is approximately similar to sea-salt tracers in WAIS Divide
450 (Sigl et al., 2016), and a few months earlier than peak values in Law Dome (Curran et al., 1998).
451 During the most recent period (1900-1990 CE), we observe a summer peak in the average
452 seasonal conductivity signal, which is not present in the calcium record. This is likely the steady
453 summer contribution from biogenic acidity, the seasonality of which being sufficiently
454 prominent to show up in seasonal averages of conductivity in the top part of the core.

455 **6.3. Black carbon**

456 Seasonal deposition of black carbon (BC) in Antarctic snow is primarily driven by biomass
457 burning and fossil fuel combustion in the Southern Hemisphere, modulated by changes in
458 efficiency of the long-range atmospheric transport (Bisiaux et al., 2012). Southern Hemispheric
459 fossil fuel emissions have increased since the 1950s (Lamarque et al., 2010), but are believed to
460 be a minor contributor to total black carbon deposition in Antarctica (Bauer et al., 2013).

461 Biomass burning in the Southern Hemisphere peaks towards the end of the dry season, e.g. late
462 summer (Schultz et al., 2008). Given the distinct annual signal in the black carbon record (Fig.
463 8j-l), StratiCounter was set up to assign peaks in BC a nominal date of January 1st (mid-
464 summer). We note that peaks in BC approximately coincide with peaks in acidity (similar to
465 observed in WAIS Divide), thus ensuring consistency of nominal dates throughout the core.
466 Minimum concentrations of BC are reached in Austral winter (June/July).

467 The annual signal in black carbon changes with depth in the RICE core. During the 20th century,
468 annual cycles exist, but are not very prominent (Fig. 8j). Prior to 1900 CE, the signal is much
469 more distinct, with larger seasonal amplitude as well as higher annual mean concentrations (Fig.
470 8k-l). A recent decrease in BC concentrations has been observed also in the WAIS Divide and
471 Law Dome ice cores, and attributed to a reduction in biofuel emissions from grass fires (Bisiaux
472 et al., 2012). At WAIS Divide and Law Dome, however, the shift takes place several decades
473 later than observed in RICE.

474 With increasing depth in the ice core, thinner annual layers cause the amplitude of the seasonal
475 signal to slowly be reduced. Yet, aided by the high effective depth resolution of the black carbon
476 record, the seasonal cycle persists to great depths in the RICE core, with the deepest part of the
477 layer-counted RICE17 timescale primarily relying on the annual signal in this parameter.

478 **6.4. Dust**

479 The seasonal pattern in insoluble dust particle concentrations showed a weak annual signal,
480 with a tendency to peak in summer. The simultaneous deposition of black carbon and dust is
481 consistent with both tracers arriving via long-range transport from southern hemispheric
482 continental sources.

483 **7. The layer-counted RICE17 chronology**

484 The layer-counted timescale was constructed back to 700 BCE (0-343.72 m), and it forms the
485 most recent part of the Roosevelt Island Ice Core Chronology 2017 (RICE17). It is an
486 independent timescale, constrained only by a few well-known historical events over the last
487 hundred years. Its independence is reflected in the timescale uncertainty: Age confidence
488 intervals show an approximately linear increase with depth (Fig. 9b), reaching a maximum age
489 uncertainty of ± 45 years (95% confidence) at 700 BCE.

490 RICE17 was evaluated by comparing to the annual-layer-counted WD2014 chronology from
491 WAIS Divide (Sigl et al., 2015, 2016). Timescale comparison was aided by the relative
492 proximity of the two ice cores, and accomplished using two complementary approaches: 1)
493 matching multi-decadal variations in the RICE methane record to a similar record from WAIS
494 Divide; and 2) by matching volcanic marker horizons in the two cores. The two matching
495 procedures were performed independently, and are described in the following sections.

496 Volcanic matching allows very precise age comparisons, but suffers from the risk of incorrect
497 event attribution. Erroneous alignment is less likely to occur when matching records of methane
498 concentration variability. This approach does not allow as high precision, however, due to the
499 multi-decadal nature of the methane variations, as well as the need to account for the gas-age-
500 ice-age difference. Combining the two lines of evidence, the methane match points were used
501 to confirm the independently-obtained volcanic match points, and to validate the absolute ages
502 of the timescale (relative to WD2014). A high-precision comparison to WD2014 was achieved
503 based on the volcanic matches, allowing an in-depth quality assessment of the RICE17
504 chronology.

505 **7.1. Timescale validation using multi-decadal variability in methane** 506 **concentrations**

507 Centennial-scale variations in methane concentrations observed in the RICE gas records can
508 also be found in similar records from WAIS Divide (Mitchell et al., 2011; WAIS Divide Project
509 Members, 2015). Stratigraphic matching of these records allowed a comparison of the
510 respective ice-core timescales.

511 The gas records from RICE and WAIS Divide were matched using a Monte Carlo technique
512 reported in Lee et al. (2018). The feature-matching routine employed discretely-measured
513 records of methane as well as the isotopic composition of molecular oxygen ($\delta^{18}\text{O}_{\text{atm}}$). Over
514 recent millennia, however, the $\delta^{18}\text{O}_{\text{atm}}$ concentrations have been stable, and hence provided
515 minimal matching constraints. An average spacing of 26 years between successive RICE
516 methane samples contributed to the matching uncertainty. The matching routine identified 18
517 match-points over the past 2700 years, i.e. an average spacing of 150 years. Subsequent visual
518 comparison of the methane profiles suggested minor manual refinements of the match-points
519 (8 years on average, maximum 23 years; all within the uncertainty of the automated matching).
520 These adjustments resulted in a slightly improved fit.

521 Through the methane feature matching, WAIS Divide ages could be transferred to the RICE
522 gas records, i.e. provide an estimate for the RICE gas ages. During the snow densification
523 process, there is a continuous transfer of contemporary air down to the gas lock-in depth,
524 resulting in an offset (Δ_{age}) between the ages of ice and gas at a given depth (Schwander and
525 Stauffer, 1984). To obtain the corresponding ice-core ice ages relevant for this study, Δ_{age} was
526 calculated using a dynamic Herron-Langway firn densification model (Herron and Langway,
527 1980) following Buizert et al. (2015). The approach is described in detail in Lee et al. (2018).
528 The model is forced using a site temperature history derived from the RICE stable water
529 isotopes, and the firn column thickness is constrained by the isotopic composition of molecular
530 nitrogen ($\delta^{15}\text{N}$ of N_2). In addition to Δ_{age} , this formulation of the Herron-Langway
531 densification model produces as output a low-resolution accumulation rate history (section 8.3).

532 Compared to most other Antarctic sites, the relatively high surface temperature and
533 accumulation rate at Roosevelt Island give rise to low Δ_{age} values (averaging 160 years over
534 recent millennia) associated with small uncertainties (~ 36 years; 1σ). Combined with the feature
535 matching uncertainty (average: 48 years), total age uncertainty (1σ) in the transfer of WD2014
536 to the RICE core is on average 64 years (maximum: 101 years) over the last 2700 years.

537 The RICE17 timescale is consistent with the WD2014 age of the methane match points (Fig.
538 9b). Based on the automatic matching routine, agreement of RICE17 to the gas-matched
539 WD2014 ages is better than 33 years for all age markers, with a root-mean-square (RMS)
540 difference of 17 years. Agreement between the two timescales is even better when using the
541 manually-adjusted match-points, for which the RMS difference is reduced to 13 years. We
542 observe, however, that all methane match points below 275 m are associated with older ages in
543 WD2014 than in RICE, suggesting a small bias in the deeper part of RICE17.

544 **7.2. Timescale evaluation from volcanic matching**

545 Using the layer counts in RICE17 as guide, volcanic horizons identified in RICE could be linked
546 to the WAIS Divide volcanic record (Sigl et al., 2013, 2015), allowing a detailed comparison
547 of their respective timescales. However, a high background level of marine biogenic sulfuric
548 acids precluded a straight-forward identification of volcanic eruptions in the RICE records.
549 Based on multiple volcanic proxy records, including two new volcanic tracers described below,
550 match points were found by identifying common sequential patterns of acidity spikes in the two
551 cores.

552 **7.2.1. New and conventional ice-core tracers for volcanic activity**

553 With its coastal location and low altitude, the RICE drilling site receives significant seasonal
554 influx of sulfuric acids from biological oceanic sources. Biogenic peak values of up to 200ppb
555 non-sea-salt sulfate are of the same order as the expected sulfate deposition from large volcanic
556 eruptions, causing the seasonal signal to partly obscure the episodic deposition of sulfuric acids
557 from volcanic eruptions. Volcanic signals appeared more distinct in the acidity record (Fig. S4),
558 primarily due to the higher resolution of this record.

559 Traditional volcanic ice-core tracers, ECM and sulfur, were not sufficient for identifying
560 volcanic horizons. The ECM record was very noisy, with few peaks extending above the noise
561 level. Resolution of the discretely-sampled sulfur record was low (below 67m: 5 cm, i.e. <4
562 samples/year), and it was therefore most valuable in the top. Even here, large volcanoes only
563 left a vague imprint in form of slightly increased sulfur levels over a multi-year period (e.g. Fig.
564 10a), with their most distinct feature being elevated sulfur concentrations also during winter.
565 Detection of volcanic horizons in the RICE core therefore primarily relied on two new high-
566 resolution tracers for volcanic activity: direct measurements of total acidity (Kjær et al., 2016)
567 and estimated non-sea-salt liquid conductivity.

568 Peaks in the RICE liquid conductivity record were caused primarily by sea salts, and thus this
569 record could not on its own be used as volcanic tracer. However, from the close similarity of
570 the conductivity and the mostly sea-salt-derived calcium record (e.g. Fig. 6), we could extract
571 a signal of non-sea-salt conductivity, obtained as the conductivity-to-calcium excess ($\text{nss-conductivity} = \text{conductivity} - (a \cdot [\text{Ca}^{2+}] + b)$, with a and b calculated from linear regression).
572 Being a secondary product, this tracer is prone to measurement errors, calibration and co-
573 registration uncertainties, and further complicated by differences in measurement resolution.
574 We therefore always double-checked by direct comparison between the two records (Fig. 10a;
575 green and grey lines), allowing peaks caused by misalignment and obvious measurement issues
576 to be identified. We observed high consistency between peaks in the non-sea-salt conductivity
577 and the total acidity records.
578

579 A sequence of volcanic signals is shown in Figure 10a. Additional sections are found in the
580 supplementary (S5). Compared to acidic peaks resulting from unusually high biogenic summer
581 activity, volcanic imprints could be distinguished as more prominent and/or broader features.
582 Small and short-lived volcanic eruptions, however, were not easily identified.

583 **7.2.2. The Pleiades: A tephra-chronological marker horizon**

584 A visible tephra layer was found in RICE at 165m depth, with a RICE17 age of 1251.5±13 CE.
585 Geochemistry of the tephra particles is consistent with an eruption from the Pleiades (Kurbatov
586 et al., 2015), a volcanic group located in Northern Victoria Land, Antarctica (Fig. 1). Tephra of
587 similar geochemistry has been found in several other Antarctic cores dated to approximately
588 the same time, including WAIS Divide (1251.6±2 CE; Dunbar et al. 2010) and Talos
589 Dome/TALDICE (1254±2 CE; Narcisi, Proposito, and Frezzotti 2001; Narcisi et al. 2012). The
590 Pleiades tephra horizon allowed a firm volcanic matching of the RICE and WAIS Divide ice
591 cores at this depth (Fig. 10).

592 The Pleiades tephra horizon was used to select the optimal settings for the StratiCounter
593 algorithm, seeking to reproduce the WD2014 age of the tephra layer as well as possible. The
594 observed compliance of the two age-scales at this depth is therefore to be expected. However,
595 we note that our use of this layer as chronological marker had little impact on the resulting
596 RICE17 timescale: All StratiCounter solutions produced very similar ages for the tephra
597 horizon, and, within the age-scale uncertainties, all were in agreement with the WD2014 age of
598 the tephra.

599 **7.2.3. Volcanic matching to WAIS Divide**

600 Based on the layer counts in RICE17, sequences of volcanic horizons in RICE were matched
601 to the WAIS Divide volcanic record (Sigl et al., 2013, 2015). Using an approach similar to the
602 one applied in e.g. Svensson et al. (2013), the matching relied on identifying successive
603 volcanic events in the two cores with similar age spacing (within the associated uncertainties),
604 according to their respective timescales (Fig. 10, see also Supplement S5). By taking advantage
605 of the information contained within the annual layer counting, we were able to identify common
606 patterns of volcanic spikes in the two cores, allowing a unique match between them (Table 2).

607 Taking this approach was especially important due to the risk of confounding volcanic and
608 biogenic signals in the RICE records. Indeed, for some sections an unequivocal sequence could
609 not be identified; Sections with too few or too many closely-spaced acidity spikes in either core
610 were particular problematic. Most match points are associated with peaks exceeding two
611 standard deviations of the overall variability of the record (Table 2). However, also some
612 smaller peaks were useful, where these formed part of a matching sequence of volcanic events.
613 Multiple additional events in the RICE records of likely volcanic origin are not included in
614 Table 2, since they could not be unambiguously matched to a peak in WAIS Divide.

615 The volcanic matching was in excellent agreement with the independently-obtained methane
616 matching, especially when using the manually-adjusted match points (Fig. 9b). A majority of
617 the volcanic links identified between the RICE and WAIS Divide ice cores have previously
618 been classified as bipolar signals, originating from large tropical volcanoes (Sigl et al., 2013,
619 2015). This further strengthens our trust in the volcanic matching, since these large eruptions
620 usually deposit acids over an extended area and period, and therefore are expected to exist also
621 in the RICE volcanic records.

622 **7.2.4. Quality assessment of RICE17**

623 The volcanic matching to WAIS Divide allowed a detailed evaluation of RICE17. The WD2014
624 counting uncertainty is merely 7 years over the last 2700 years, much less than the uncertainty
625 associated with RICE17, and we hence consider it to be the more accurate of the two. Within
626 their respective uncertainties, the RICE17 and WD2014 chronologies are in full agreement at
627 all volcanic marker horizons (Table 2; Fig. 9b). Indeed, the age differences are much less than
628 the accumulated RICE17 age uncertainties. We hence conclude that the inferred confidence
629 bounds on the RICE17 chronology are reliable, if somewhat conservative.

630 Agreement between the two ice-core timescales is particularly remarkable down to 285 m (~150
631 CE). For this most recent part of the RICE17 timescale, the age discrepancy is less than 7 years
632 at all marker horizons, with a RMS age difference of 3 years. Below 285 m, the volcanic
633 matches indicate that RICE17 has a slight (~3%) bias towards younger ages. This is
634 corroborated by the methane match points (section 7.1). At 285 m, the effective depth resolution
635 of the CFA impurity records (1-2 cm) becomes marginal compared to the annual layer
636 thicknesses (7 cm at 285 m), and we suspect that this has caused the thinnest fraction of annual
637 layers to be indiscernible in the ice core records.

638 Consequently, the deepest section of the layer-counted RICE17 chronology slowly diverges
639 from WD2014, reaching a maximum age difference of 30 years at the oldest identified volcanic
640 marker horizon (343.3 m, 691 BCE \pm 45 years; Table 2). This age offset is of similar magnitude
641 to the uncertainty of the methane-derived RICE17 ages at this depth.

642 **8. Roosevelt Island accumulation history**

643 Annual layer thicknesses in the RICE ice core smoothly decrease with depth, starting from more
644 than 40 cm at the surface to ~6 cm at 344 m (Fig. 9a). After corrections for density changes and
645 ice flow thinning of annual layers with depth (section 5), an annual accumulation rate history
646 for Roosevelt Island over the last 2700 years was obtained (Fig. 11f).

647 **8.1. Long-term accumulation trends**

648 Mean accumulation rates at Roosevelt Island over the entire 2700 year period was 0.25 ± 0.02 m
649 w.e. yr^{-1} . From 700 BCE to ~1300 CE, the accumulation rate at Roosevelt Island shows a
650 slightly increasing trend (Fig. 11f; Table 3), and in 1250 CE, the 20-year running mean
651 accumulation rate reached its maximum over the last 2700 year (0.32 m w.e. yr^{-1}). Since then,
652 accumulation rates have decreased: very slowly until ~1650 CE, then more rapidly (0.10
653 mm/yr^2 from 1650-1965 CE; Table 3). A continued acceleration in the decline of accumulation
654 rates is observed towards the present. Change points and trend estimates with their associated
655 uncertainties were identified using a break function regression analysis (Mudelsee, 2009).
656 However, the high inter-annual variability in accumulation rates prohibited very accurate
657 determination of the breakpoints.

658 **8.2. Significant decrease in recent accumulation rates**

659 The Roosevelt Island accumulation history reveals a distinct and rapid accumulation decrease
660 in recent decades: Since the mid-1960s, the annual accumulation has decreased with a rate
661 corresponding to 0.8 mm/yr^2 , i.e. 8 times faster than over previous centuries. We note, however,
662 that the relatively short time period for conducting the trend analysis, combined with the large
663 inter-annual variability in accumulation rates, causes significant uncertainty in the precise
664 timing of the change-point as well as the trend estimate.

665 Considering the period since 1700 CE (Fig. 12), the lowest decadal mean value of the
666 accumulation rate is observed in the 1990s (0.194 ± 0.001 m w.e. yr^{-1}). Except for very low
667 accumulation rates during the 1850s and 1800s, the remaining top six decades of lowest mean
668 accumulation take place after 1950 CE (Table 4). Indeed, over the last 50 years, only one decade
669 (1960s) stands out as not having experienced below-average accumulation at Roosevelt Island.

670 The current accumulation rate at Roosevelt Island of 0.210 ± 0.002 m w.e. yr^{-1} (average since
671 1965 CE, $\pm 2\sigma$) is 34% less than the peak accumulation rates around 1250 CE, and 16% below
672 the average of the last 2700 years.

673 **8.3. Comparison to the gas-based accumulation rates**

674 The RICE17 accumulation history is in reasonable agreement with the low-resolution
675 accumulation rate output from the dynamic Herron-Langway firn densification model (Fig. 11f,
676 dashed line). The gas-based accumulation rate history does not resolve high-frequency
677 variations, but shows a slow increase in accumulation rates of 0.02 mm/yr^2 , similar to the trend
678 obtained from the annual layer thicknesses prior to 1300 CE. However, in contrast to the
679 accumulation rate history derived here, the firn-based accumulation rates continue to increase
680 until present. Further, the absolute value of the inferred gas-based accumulation rates tend to
681 generally underestimate the accumulation rates by $\sim 0.04 \text{ m w.e. yr}^{-1}$ (16%).

682 We speculate that the discrepancies may have to do with the shift in RICE water isotope levels
683 occurring around 1500 CE (Fig. 11g), which in the firn model is used to represent temperature
684 change. It has been suggested that this shift is due to other factors than temperature (e.g. changes
685 in atmospheric circulation patterns and/or regional sea ice extent (Bertler et al., 2018), and the
686 shift also coincides with commencement of the divide migration period). By using δD to
687 estimate temperature change, the firn densification model will produce an increase in
688 accumulation rates towards present in order to preserve a constant thickness of the firn column,
689 as indicated by relatively steady values of $\delta^{15}\text{N-N}_2$ (Fig. 11f, black dots). Further, the model
690 showed a tendency to underestimate the firn column thickness during the earlier part of the
691 period, which may explain the generally lower level of the modelled accumulation rates here.

692 **8.4. Spatial consistency in recent accumulation rates**

693 Spatial representativeness of the RICE accumulation rates was evaluated by comparing year-
694 to-year profiles of layer thicknesses obtained for the overlap sections of the three available
695 cores: RICE main core, RICE-12/13-B, and RID-75 (Fig. 13), with RID-75 located less than 1
696 km away from the two RICE cores. All cores were corrected for density changes and ice flow
697 thinning using the density and thinning profile from the main RICE core.

698 Annual accumulation records from the three cores are very strongly correlated (correlation
699 coefficients ranging between 0.85 and 0.87), indicating the spatial accumulation pattern across
700 Roosevelt Island to be stable through recent time. The spatial consistency of snow deposition
701 at Roosevelt Island is corroborated by the agreement between their measured water isotope
702 records (Fig. 5a). We may therefore disregard depositional noise, and consider the temporal
703 variability in RICE annual layer thicknesses as representative of local snow accumulation.

704 This consistency in accumulation history is in contrast to a high spatial variability in mean
705 accumulation rates across Roosevelt Island ice divide. Repeat surveys over three years (2010-
706 2013) of 144 survey stakes set across Roosevelt Island showed a strong spatial gradient in snow
707 accumulation across the ice divide: Accumulation rates of up to $0.32 \text{ m w.e. yr}^{-1}$ were measured
708 on the north eastern flank, decreasing to $0.09 \text{ m w.e. yr}^{-1}$ on the south western flank (Bertler et
709 al., 2018). In accordance with these stake measurements, the absolute accumulation rate is
710 found to be significantly less ($\sim 7\%$) for RID-75 than for the RICE cores. Differences in
711 accumulation rate between the two RICE cores were insignificant. Spatial variability in mean
712 accumulation rates, combined with different averaging periods, may explain why previous
713 estimates of Roosevelt Island accumulation rates have varied quite significantly (Bertler et al.,
714 2018; Conway et al., 1999; Herron and Langway, 1980; Kingslake et al., 2014).

715 The representativeness of the Roosevelt Island accumulation rates is corroborated by high
716 spatial correlation of the RICE accumulation rates to gridded ERA-interim precipitation data
717 during recent decades (Bertler et al., 2018). These results suggest that precipitation variability

718 at Roosevelt Island, as observed in RICE, is representative for an extended area, which includes
719 the Ross Ice Shelf, the Southern Ross Sea, and the western part of West Antarctica.

720 **8.5. Influence of ice divide migration on the accumulation history**

721 The recent period (~1500-1750 CE) of divide migration at Roosevelt Island may impact
722 interpretation of the climate records from the RICE core. Ice recovered in the deeper part of the
723 RICE core, deposited before divide migration, have originated west of the ice divide. Present
724 accumulation rates show a distinct decrease on the downwind (western) side of the ice divide
725 with a gradient of $\sim 5 \cdot 10^{-3}$ m w.e./km yr⁻¹ (Bertler et al., 2018), although muted around the
726 summit area. Assuming a stable snowfall pattern through time relative to the divide, the divide
727 migration would have caused reduced accumulation rates to be observed during the early part
728 (until 1500 CE) of the RICE accumulation history. With the ice originating up to 500m west of
729 the divide at time of deposition, our estimates of Roosevelt Island accumulation rates during
730 this early period may therefore have a small negative bias of up to $2.5 \cdot 10^{-3}$ m w.e. yr⁻¹.

731 Correcting for the influence of ice divide migration, the main impact on the Roosevelt Island
732 accumulation history is an earlier onset of the period with more rapid decrease in accumulation
733 rates. The differences are small, however, and the overall pattern of trends in accumulation rate
734 through time remains the same. In particular, ice divide migration has no impact on
735 accumulation rate trends observed before and after the migration period.

736 **Discussion**

737 **9. The RICE accumulation history in a regional perspective**

738 **9.1. Past accumulation trends across West Antarctica**

739 Regional differences in accumulation, from Northern Victoria Land across West Antarctica to
740 Ellsworth Land, may be evaluated by accumulation reconstructions based on ice core records
741 (Fig. 11).

742 The RICE accumulation history (Fig. 11f) is much more variable on inter-annual and decadal
743 scales than the accumulation rate reconstruction from e.g. WAIS Divide (Fig. 11d). Snowfall
744 at Roosevelt Island is dominated by large and episodic precipitation events (Emanuelsson et al.,
745 2018), which likely contributes to the high inter-annual variability in RICE accumulation rates.
746 A highly dynamic synoptic-scale system brings this precipitation to Roosevelt Island: Positive
747 RICE precipitation anomalies have been linked to the increased occurrence of Eastern Ross
748 Sea/Amundsen Sea blocking events associated with a weak state of the quasi-stationary
749 Amundsen Sea Low (ASL) pressure system. These blocking events impede the prevailing
750 westerly winds, and direct on-shore winds towards the Eastern Ross Sea, thereby increasing the
751 precipitation at Roosevelt Island and Western Marie Byrd Land (Emanuelsson et al., 2018).

752 Only the WAIS Divide and RICE ice cores are available for evaluating multi-millennial-scale
753 accumulation trends and corresponding change points in West Antarctica. Over the past 2700
754 years, WAIS Divide accumulation rates (Fudge et al., 2016) have continuously decreased from
755 a level approximately 25% higher than today (Fig. 11d). Accumulation rates declined slowly (-
756 0.01 mm/yr²) until around 900 CE, after which the decline became more rapid (-0.04 mm/yr²).
757 This change took place a few centuries before the trend in RICE accumulation rates turned from
758 positive to negative (1300 CE). Covering the last 800 years, the Talos Dome accumulation
759 record (Fig. 11c) shows a relatively constant level during this early period, albeit with large
760 decadal variability (Stenni et al., 2002).

761 Considering accumulation changes over the last century, more ice-core accumulation records
762 are available from across West Antarctica; from Victoria Land through to Ellsworth Land. Most
763 West Antarctic ice cores display decreasing accumulation rates over recent decades, but timing
764 and strength of the decrease is location-dependent. The strongest and most recent decrease is
765 observed at RICE (rate change at 1965 CE, this work), with Siple Dome accumulation rates
766 starting to decrease slightly later (1970 CE, Fig. 11e; Kaspari et al., 2004). The WAIS Divide
767 site displays the latest and weakest change of rate (ca. 1975 CE; estimated from nearby firn
768 cores; Burgener et al., 2013). An extension of the Talos Dome accumulation record to 2010CE
769 using snow stakes (Fig. 11c), suggests a recent decrease in accumulation rate also at this
770 location (Frezzotti et al., 2007). In contrast, significant increases in accumulation rates are
771 observed in ice cores from Ellsworth Land, where accumulation rates have shown a steady and
772 marked increase during the 20th century (Fig. 11b, Thomas et al. 2015).

773 The difference in accumulation rate trends across West Antarctica may to a large extent be
774 explained by changes in location and intensity of the ASL over time. The ASL influences
775 precipitation rates in a dipole pattern: By reducing the number of blocking events, a strong state
776 of the ASL leads to less precipitation over the Ross Ice Shelf area, and greater precipitation
777 over Ellsworth Land and the Antarctic Peninsula (Emanuelsson et al., 2018; Raphael et al.,
778 2016). Thus, imposed on West Antarctic-wide accumulation trends, the RICE accumulation
779 history likely reflects the state of the ASL back in time. The precipitation dipole is centered at
780 the West Antarctic ice divide. Hence, the WAIS Divide ice core should be minimally influenced
781 by the strength of the ASL, and may therefore be most representative for West Antarctica as a
782 whole (Fudge et al., 2016). The Northern Victoria Land region, located west of the Ross Ice
783 Shelf, appears to be relatively unaffected by this ASL-induced dipole effect in precipitation
784 which influences Ellsworth Land and West Antarctica. The recent accumulation decrease
785 observed at Talos Dome has been suggested to be caused partly by increased wind-driven
786 sublimation after deposition, due to an increase in mean wind velocities associated with the
787 deepened ASL (Frezzotti et al., 2007).

788 **9.2. Connection to sea ice variability in the Ross Sea**

789 Throughout the satellite era, RICE accumulation rates are strongly correlated with sea ice extent
790 in the Ross-Amundsen Sea (Jones et al., 2016): Years of reduced sea ice extent are associated
791 with higher accumulation of more isotopically enriched snow and above-normal air
792 temperatures (Bertler et al., 2018).

793 The expansion of sea ice in the Ross Sea during recent decades has taken place concurrently
794 with a marked reduction of sea ice in the Bellingshausen Sea (Comiso and Nishio, 2008), and
795 both trends have been associated with a strengthening of the ASL: The deepened pressure
796 system causes warm poleward-flowing air masses to cross the Bellingshausen Sea, while the
797 returning cold air passes over the Ross Sea, allowing conditions favorable for sea ice expansion
798 (Hosking et al., 2013; Raphael et al., 2016; Turner et al., 2016). The strength of the ASL affects
799 RICE accumulation rates (section 9.1), with a deep pressure system causing less precipitation
800 at Roosevelt Island. In addition, an extended regional sea ice cover reduce the availability of
801 local moisture sources. With ~40-60% of the precipitation arriving to Roosevelt Island
802 originating from local sources in the Southern Ross Sea (Tuohy et al., 2015), the relationship
803 between sea ice extent and precipitation rate at Roosevelt Island may also be ascribed a longer
804 distillation pathway of moist air masses during periods of extended sea ice (Kuttel et al., 2012;
805 Noone and Simmons, 2004).

806 The rapid recent decline in Roosevelt Island accumulation rates likely reflects the recent
807 increase in regional sea ice extent, and we hence suggest 1965 CE to mark the modern onset of
808 rapid sea ice expansion in the region. Further investigations are required to determine if the
809 strong relationship between Roosevelt Island accumulation rates and Western Ross Sea sea-ice
810 extent holds over longer timescales. However, the decline in RICE accumulation rates observed
811 since 1300 CE is consistent with previous research indicating that the present increase in sea
812 ice extent in the Ross-Amundsen Seas is part of a long-term trend, having lasted at least the
813 past 300 years (Thomas and Abram, 2016).

814 **9.3. Large-scale circulation changes and implications for recent and** 815 **future trends in Roosevelt Island accumulation**

816 The ASL is sensitive to large-scale circulation patterns, in particular the Southern Annual Mode
817 (SAM) [positive SAM: stronger ASL (e.g. Hosking et al., 2013)] and via teleconnections to the
818 tropical El Niño-Southern Oscillation (ENSO) [stronger ASL during La Niña phase (e.g. Yuan
819 & Martinson 2000)], and the degree to which the two are acting in phase (Clem and Fogt, 2013).
820 A recent strengthening of SAM has been reported (Marshall 2003), consistent with the recent
821 deepening of the ASL (Raphael et al. 2016).

822 It is not clear whether the recent trends in ASL and Ross Sea sea-ice extent can be ascribed to
823 natural variability. Some studies have attributed the positive trend of SAM in recent decades to
824 Antarctic stratospheric ozone depletion and/or global warming from greenhouse gas emissions
825 (Kushner et al., 2001; Turner et al., 2009), thus suggesting that anthropogenic forcing may play
826 a role. In the future, the competing effects of the two (Arblaster et al., 2011) may define the
827 future state of the ASL, and thereby the accumulation trends observed at Roosevelt Island and
828 across West Antarctica.

829 Most other coastal Antarctic sites have experienced a significant increase (~10%) in
830 accumulation rates since the 1960s (Frezzotti et al., 2013). The broad similarities and
831 differences noted here raise the question of whether West Antarctic accumulation, as a whole,
832 is decreasing, or whether the observed trends merely represent a redistribution of precipitation.
833 It highlights the issue that the current trend in total Antarctic mass balance can only be fully
834 understood pending large spatial data coverage.

835 **10. The RICE volcanic record**

836 **10.1. Bias towards regional volcanism**

837 The volcanic proxy records from RICE were significantly different from those from e.g. WAIS
838 Divide. At Roosevelt Island, the high background levels of marine sulfate efficiently masked
839 the presence of sulfate from volcanic eruptions. Furthermore, the RICE acidity records
840 contained a large number of significant peaks without counterpart in WAIS Divide. While some
841 of these may be caused by extreme seasonal influx of marine biogenic sulfuric acids, others
842 may have been produced by regional volcanism.

843 Apart from sulfate, many volcanoes emit acidic compounds based on halogens, e.g. bromine,
844 chlorine and fluoride. The halide acids are highly soluble, and will be removed from the
845 atmosphere relatively quickly during transport. Hence, they will contribute to increased ice
846 acidity in ice cores located close to the eruption site, whereas only sulfate is deposited from
847 distant volcanic eruptions (e.g. Clausen et al., 1997). By using acidity as the primary volcanic
848 tracer (instead of sulfur), we would therefore expect the resulting volcanic record to be
849 particularly sensitive to regional volcanism. This may be a disadvantage of using acidity as

850 volcanic tracer, since a high number of regional volcanic horizons will tend to complicate
851 volcanic matching to other cores.

852 Such geographical bias may be especially important for the Roosevelt Island ice-core records,
853 since there is a prevalence of quiescent regional volcanism with relatively high halogen content
854 in West Antarctica (Zreda-Gostynska et al., 1997). Indeed, preliminary investigations suggest
855 that the RICE volcanic records may be biased towards regional volcanism: Comparing down-
856 sampled acidity to the discrete sulfur measurements, we observed a tendency towards a larger
857 relative size of peaks in acidity for volcanic horizons that were not classified as originating
858 from far-field eruptions. Some of the peaks distinctly observed in the RICE acidity records, but
859 not present in the WAIS Divide sulfur records, may therefore be due to regional volcanism.
860 This may be part of the explanation why the volcanic records from the two sites are so different.

861 **10.2. Dipole effect in deposition of volcanic tracers across West** 862 **Antarctica**

863 Differences in snow deposition across West Antarctica, influenced by the ASL, may further
864 complicate volcanic matching between ice cores in this region. The ASL dipole acts to direct
865 storm systems either toward the Antarctic Peninsula/Ellsworth Land region, or toward the
866 western Marie Byrd Land/Ross Ice Shelf region. As these storm tracks are associated with
867 snowfall and wet deposition of ions, this is likely to favor deposition and preservation of
868 volcanic signals in one location (e.g. Antarctic Peninsula) at expense of the other (RICE, Siple
869 Dome).

870 An anti-phase in snow accumulation may thus be part of the explanation for the difference
871 between the WAIS Divide and RICE volcanic records. While most of the major volcanic signals
872 in WAIS Divide also exist in RICE, they are not necessarily associated with a prominent signal.
873 Absence of volcanic signal in the RICE core from large far-field volcanic eruptions may be due
874 to a particularly strong ASL state at the time, directing precipitation and sulfate ions away from
875 Roosevelt Island. A detailed comparison of volcanic records from multiple ice cores is required
876 to evaluate the importance of the ASL for deposition of volcanic tracers across West Antarctica.

877 **10.3. Volcanic synchronization of low-elevation coastal ice cores**

878 A range of obstacles were overcome to carry out volcanic identification in the RICE core.
879 Similar difficulties will likely challenge volcanic synchronization for other low-elevation
880 coastal Antarctic ice cores (e.g. Philippe et al., 2016), for which many drilling projects are
881 planned within the near future. The methods proposed here may be relevant also for these cores.

882 Robust volcanic matching of RICE and WAIS Divide was possible only by the aid of accurate,
883 high-resolution ice-core timescales for both cores. This demonstrates the importance of
884 building an Antarctic-wide network of accurately-dated volcanic reference horizons, based on
885 tephra, sulfate and acidity. Particular emphasis should be placed on the production of annually-
886 counted timescales for Antarctic ice cores, especially as new and/or improved measurement
887 methods allow the production of high-resolution impurity records for relatively high-
888 accumulation Antarctic sites, such as RICE.

889 **Conclusions**

890 The upper part of the RICE ice core from Roosevelt Island, Ross Ice Shelf, West Antarctica,
891 was dated by annual layer counting back to 700 BCE based on multiple high-resolution impurity
892 records. The timescale covers a period of stable ice flow after establishment of an ice divide at
893 Roosevelt Island. The chronology was validated by comparison to the timescale from the WAIS

894 Divide ice core, West Antarctica, by matching sequences of volcanic events visible primarily
895 in direct measurements of ice-core acidity and non-sea-salt conductivity. The maritime
896 environment at Roosevelt Island gave rise to challenging conditions for identifying volcanic
897 signatures in the ice core, and the volcanic matching was confirmed by matching centennial-
898 scale variability in atmospheric methane concentrations measured in the two ice cores. The
899 RICE17 and WD2014 timescales were found to be in excellent agreement.

900 Based on the layer thickness profile, we produced an annual accumulation record for Roosevelt
901 Island for the past 2700 years. Similar accumulation histories are observed in three Roosevelt
902 Island ice cores covering recent times, giving confidence that RICE is a reliable climate archive
903 suitable for further understanding of climate variability across West Antarctica.

904 Roosevelt Island accumulation rates were slightly increasing from 700 BCE until 1300 CE,
905 after which accumulation rates have consistently decreased. Current accumulation trends at
906 Roosevelt Island indicate a rapid decline of 0.8 mm/yr², starting in the mid-1960s. The modern
907 accumulation rate of 0.21 m w.e yr⁻¹ (average since 1965CE) is at the low extreme of observed
908 values during the past several thousands of years. The low present-day accumulation rate has
909 been linked to a strengthening of the Amundsen Sea Low, and expansion of sea ice in the
910 Western Ross Sea. The current increase of sea ice in the Ross Sea is therefore likely part of a
911 long-term increasing trend, although the rapid increase since the mid-1960s may have an
912 anthropogenic origin.

913 **Data availability:**

914 The following data will be made available on the Centre for Ice and Climate website
915 (<http://www.iceandclimate.nbi.ku.dk/data/>) as well as public archives PANGAEA and NOAA
916 paleo-databases: RID-75 isotope and beta-activity records; RICE-12/13-B and RID-75
917 accumulation rates; RICE17 timescale; RICE accumulation rates; and volcanic match points
918 between RICE and WAIS Divide. Roosevelt Island GPS and radar data are archived at the U.S.
919 Antarctic Program Data Center, available
920 at: <https://gcmd.gsfc.nasa.gov/search/Metadata.do?entry=USAP0944307&subset=GCMD>.

921 **Acknowledgements**

922 This work is a contribution to the Roosevelt Island Climate Evolution (RICE) Program, funded
923 by national contributions from New Zealand, Australia, Denmark, Germany, Italy, China,
924 Sweden, UK and USA. The main logistic support was provided by Antarctica New Zealand
925 (K049) and the US Antarctic Program. We thank all the people involved in the RICE logistics,
926 fieldwork, sampling and analytical programs. The Danish contribution to RICE was funded by
927 the Carlsberg Foundation's North-South Climate Connections project grant. The research also
928 received funding from the European Research Council under the European Community's
929 Seventh Framework Programme (FP7/2007-2013) ERC grant agreement 610055 as part of the
930 Ice2Ice project. The RICE Program was supported by funding from NSF grants (PLR-1042883,
931 ANT-0837883, ANT-0944021, ANT-0944307 and ANT-1643394) and New Zealand Ministry
932 of Business, Innovation, and Employment grants issued through Victoria University of
933 Wellington (RDF-VUW-1103, 15-VUW-131), GNS Science (540GCT32, 540GCT12) and
934 Antarctica New Zealand (K049). Figure 1 was made using Quantarctica2 (Norwegian Polar
935 Institute) basemaps and QGIS software. We acknowledge the WAIS Divide ice-core project,
936 and thank J. McConnell, Jihong Cole-Dai, and the students and staff of the ice core labs at the
937 Desert Research Institute and at South Dakota State University for providing the WAIS Divide
938 sulfate data.

939 We have presented here ice core data collected and analyzed by Henrik Clausen, Willi
940 Dansgaard, Sigfus Johnsen, Steffen Bo Hansen and Jan Nielsen under the Ross Ice Shelf Project
941 (RISP) carried out between 1973 and 1978. We acknowledge the pioneering work conducted
942 by these researchers and the ongoing international collaborations they established.

943 **References**

- 944 Abbott, P. M., Davies, S. M., Steffensen, J. P., Pearce, N. J. G., Bigler, M., Johnsen, S. J.,
945 Seierstad, I. K., Svensson, A. and Wastegård, S.: A detailed framework of Marine Isotope
946 Stages 4 and 5 volcanic events recorded in two Greenland ice-cores, *Quat. Sci. Rev.*, 36, 59–
947 77, doi:10.1016/j.quascirev.2011.05.001, 2012.
- 948 Alley, R. B., Meese, D. A., Shuman, C. A., Gow, A. J., Taylor, K. C., Grootes, P. M., White, J.
949 W. C., Ram, M., Waddington, E. D., Mayewski, P. A. and Zielinski, G. A.: Abrupt increase in
950 Greenland snow accumulation at the end of the Younger Dryas event, *Nature*, 362(6420), 527–
951 529, doi:10.1038/362527a0, 1993.
- 952 Andersen, K., Svensson, A., Johnsen, S., Rasmussen, S., Bigler, M., Röthlisberger, R., Ruth,
953 U., Siggaard-Andersen, M.-L., Steffensen, J., Dahl-Jensen, D., Vinther, B. and Clausen, H.:
954 The Greenland Ice Core Chronology 2005, 15–42ka. Part 1: constructing the time scale, *Quat.*
955 *Sci. Rev.*, 25(23–24), 3246–3257, doi:10.1016/j.quascirev.2006.08.002, 2006.
- 956 Arblaster, J. M., Meehl, G. A. and Karoly, D. J.: Future climate change in the Southern
957 Hemisphere: Competing effects of ozone and greenhouse gases, *Geophys. Res. Lett.*,
958 38(L02701), 1–6, doi:10.1029/2010GL045384, 2011.
- 959 Arienzo, M. M., McConnell, J. R., Chellman, N., Criscitiello, A. S., Curran, M., Fritzsche, D.,
960 Kipfstuhl, S., Mulvaney, R., Nolan, M., Opel, T., Sigl, M. and Steffensen, J. P.: A Method for
961 Continuous ²³⁹Pu Determinations in Arctic and Antarctic Ice Cores, *Environ. Sci. Technol.*,
962 50, 7066–7073, doi:10.1021/acs.est.6b01108, 2016.
- 963 Bauer, S. E., Bausch, A., Nazarenko, L., Tsigaridis, K., Xu, B., Edwards, R., Bisiaux, M. and
964 McConnell, J.: Historical and future black carbon deposition on the three ice caps: Ice core
965 measurements and model simulations from 1850 to 2100, *J. Geophys. Res. Atmos.*, 118(14),
966 7948–7961, doi:10.1002/jgrd.50612, 2013.
- 967 Bender, M. L., Sowers, T., Barnola, J. M. and Chappellaz, J.: Changes in the O₂/N₂ ratio of the
968 atmosphere during recent decades reflected in the composition of air in the firn at Vostok
969 Station, Antarctica, *Geophys. Res. Lett.*, 21(3), 189–192, doi:10.1029/93GL03548, 1994.
- 970 Bentley, C. R. and Giovinetto, M. B.: Ice-flow studies on the ice dome of Roosevelt Island,
971 Antarctica, *Trans. Am. Geophys. Union*, 43(3), 369–372, doi:10.1029/TR043i003p00345,
972 1962.
- 973 Bertler, N. A. N., Conway, H., Dahl-Jensen, D., Emanuelsson, D. B., Winstrup, M., Vallelonga,
974 P. T., Lee, J. E., Brook, E. J., Severinghaus, J. P., Fudge, T. J., Keller, E., Baisden, W. T.,
975 Hindmarsh, R. C. A., Neff, P. D., Blunier, T., Edwards, R., Mayewski, P. A., Kipfstuhl, S.,
976 Buizert, C., Canessa, S., Dacic, R., Kjær, H. A., Kurbatov, A. V., Zhang, D., Waddington, E.
977 D., Baccolo, G., Beers, T., Brightley, H. J., Carter, L., Clemens-Sewall, D., Ciobanu, V. G.,
978 Delmonte, B., Eling, L., Ellis, A. A., Ganesh, S., Colledge, N., Haines, S. A., Handley, M.,
979 Hawley, R. L., Hogan, C. M., Johnson, K. M., Korotkikh, E., Lowry, D. P., Mandeno, D.,
980 McKay, R. M., Menking, J. A., Naish, T. R., Noerling, C., Ollive, A., Orsi, A., Proemse, B. C.,
981 Pyne, A. R., Pyne, R. L., Renwick, J., Scherer, R. P., Semper, S., Simonsen, M., Sneed, S. B.,
982 Steig, E. J., Tuohy, A., Ulayottil Venugopal, A., Valero-Delgado, F., Venkatesh, J., Wang, F.,

- 983 Wang, S., Winski, D. A., Winton, V. H. L., Whiteford, A., Xiao, C., Yang, J. and Zhang, X.:
984 The Ross Dipole - temperature, snow accumulation, and sea ice variability in the Ross Sea
985 Region, Antarctica, over the past 2700 years, *Clim. Past*, 14, 193–214, doi:10.5194/cp-14-193-
986 2018, 2018.
- 987 Bigler, M., Svensson, A., Kettner, E., Vallelonga, P., Nielsen, M. E. and Steffensen, J. P.:
988 Optimization of high-resolution continuous flow analysis for transient climate signals in ice
989 cores, *Environ. Sci. Technol.*, 45(10), 4483–4489, doi:10.1021/es200118j, 2011.
- 990 Bisiaux, M. M., Edwards, R., McConnell, J. R., Curran, M. A. J., Van Ommen, T. D., Smith,
991 A. M., Neumann, T. A., Pasteris, D. R., Penner, J. E. and Taylor, K.: Changes in black carbon
992 deposition to Antarctica from two high-resolution ice core records, 1850-2000 AD, *Atmos.*
993 *Chem. Phys.*, 12(9), 4107–4115, doi:10.5194/acp-12-4107-2012, 2012.
- 994 Blunier, T.: Timing of Millennial-Scale Climate Change in Antarctica and Greenland During
995 the Last Glacial Period, *Science*, 291(5501), 109–112, doi:10.1126/science.291.5501.109,
996 2001.
- 997 Blunier, T., Chappellaz, J., Schwander, J., Dällenbach, A., Stauffer, B., Stocker, T. F., Raynaud,
998 D., Jouzel, J., Clausen, H. B., Hammer, C. U. and Johnsen, S. J.: Asynchrony of Antarctic and
999 Greenland climate change during the last glacial period, *Nature*, 394, 739–743,
1000 doi:10.1038/29447, 1998.
- 1001 Buizert, C., Cuffey, K. M., Severinghaus, J. P., Baggenstos, D., Fudge, T. J., Steig, E. J.,
1002 Markle, B. R., Winstrup, M., Rhodes, R. H., Brook, E. J., Sowers, T. a., Clow, G. D., Cheng,
1003 H., Edwards, R. L., Sigl, M., McConnell, J. R. and Taylor, K. C.: The WAIS Divide deep ice
1004 core WD2014 chronology - Part 1: Methane synchronization (68–31 ka BP) and the gas age–
1005 ice age difference, *Clim. Past*, 11, 153–173, doi:10.5194/cp-11-153-2015, 2015.
- 1006 Burgener, L., Rupper, S., Koenig, L., Forster, R., Christensen, W. F., Williams, J., Koutnik, M.,
1007 Miège, C., Steig, E. J., Tingey, D., Keeler, D. and Riley, L.: An observed negative trend in West
1008 Antarctic accumulation rates from 1975 to 2010: Evidence from new observed and simulated
1009 records, *J. Geophys. Res. Atmos.*, 118(10), 4205–4216, doi:10.1002/jgrd.50362, 2013.
- 1010 Clapp, J. L.: Summary and Discussion of Survey Control for Ice Flow Studies on Roosevelt
1011 Island, Antarctica, *Univ. Wisconsin Res. Rep.*, 65(1), 1965.
- 1012 Clausen, H. B., Dansgaard, W., Nielsen, J. O. and Clough, J. W.: Surface accumulation on Ross
1013 Ice Shelf, *Antarct. J. United States*, 14(5), 68–74, 1979.
- 1014 Clausen, H. B., Hammer, C. U., Hvidberg, C. S., Dahl-Jensen, D., Steffensen, J. P., Kipfstuhl,
1015 J. and Legrand, M.: A comparison of the volcanic records over the past 4000 years from the
1016 Greenland Ice Core Project and Dye 3 Greenland ice cores, *J. Geophys. Res. Ocean.*, 102(C12),
1017 26707–26723, doi:10.1029/97JC00587, 1997.
- 1018 Clem, K. R. and Fogt, R. L.: Varying roles of ENSO and SAM on the Antarctic Peninsula
1019 climate in austral spring, *J. Geophys. Res. Atmos.*, 118, 11481–11492, doi:10.1002/jgrd.50860,
1020 2013.
- 1021 Comiso, J. C. and Nishio, F.: Trends in the sea ice cover using enhanced and compatible
1022 AMSR-E, SSM/I, and SMMR data, *J. Geophys. Res. Ocean.*, 113(C02S07), 1–22,
1023 doi:10.1029/2007JC004257, 2008.

- 1024 Conway, H., Hall, B., Denton, G., Gades, A. and Waddington, E.: Past and future grounding-
 1025 line retreat of the West Antarctic ice sheet, *Science*, 286(280), 280–283,
 1026 doi:10.1126/science.286.5438.280, 1999.
- 1027 Curran, M. A. J., van Ommen, T. D. and Morgan, V.: Seasonal characteristics of the major ions
 1028 in the high-accumulation Dome Summit South ice core, Law Dome, Antarctica, *Ann. Glaciol.*,
 1029 27, 385–390, doi:10.3189/1998AoG27-1-385-390, 1998.
- 1030 Dahl-Jensen, D., Johnsen, S., Hammer, C., Clausen, H. and Jouzel, J.: Past accumulation rates
 1031 derived from observed annual layers in the GRIP ice core from Summit, Central Greenland, in
 1032 NATO ASI Series, vol. I12, edited by W. R. Peltier, pp. 517–532, Springer-Verlag Berlin
 1033 Heidelberg, doi: 10.1007/978-3-642-85016-5, 1993.
- 1034 Dansgaard, W.: Stable isotopes in precipitation, *Tellus*, 16(4), 436–468,
 1035 doi:10.3402/tellusa.v16i4.8993, 1964.
- 1036 Dee, D. P., Uppala, S. M., Simmons, A. J., Berrisford, P., Poli, P., Kobayashi, S., Andrae, U.,
 1037 Balmaseda, M. A., Balsamo, G., Bauer, P., Bechtold, P., Beljaars, A. C. M., van de Berg, L.,
 1038 Bidlot, J., Bormann, N., Delsol, C., Dragani, R., Fuentes, M., Geer, A. J., Haimberger, L.,
 1039 Healy, S. B., Hersbach, H., Hólm, E. V., Isaksen, I., Kållberg, P., Köhler, M., Matricardi, M.,
 1040 McNally, A. P., Monge-Sanz, B. M., Morcrette, J. J., Park, B. K., Peubey, C., de Rosnay, P.,
 1041 Tavolato, C., Thépaut, J. N. and Vitart, F.: The ERA-Interim reanalysis: Configuration and
 1042 performance of the data assimilation system, *Q. J. R. Meteorol. Soc.*, 137(656), 553–597,
 1043 doi:10.1002/qj.828, 2011.
- 1044 Dunbar, N. W., Kurbatov, A. V., Koffman, B. G. and Kreutz, K. J.: Tephra Record of Local
 1045 and Distal Volcanism in the WAIS Divide Ice Core, in WAIS Divide Science Meeting
 1046 September 30th-October 1st, La Jolla, CA, USA. [online] Available from:
 1047 <https://geoinfo.nmt.edu/staff/dunbar/publications/abstracts/dakk2010.html>, 2010.
- 1048 Emanuelsson, B. D., Baisden, W. T., Bertler, N. A. N., Keller, E. D. and Gkinis, V.: High-
 1049 resolution continuous-flow analysis setup for water isotopic measurement from ice cores using
 1050 laser spectroscopy, *Atmos. Meas. Tech.*, 8(7), 2869–2883, doi:10.5194/amt-8-2869-2015,
 1051 2015.
- 1052 Emanuelsson, B. D., Bertler, N. A. N., Neff, P. D., Renwick, J. A., Markle, B. R., Baisden, W.
 1053 T. and Keller, E. D.: The role of Amundsen–Bellingshausen Sea anticyclonic circulation in
 1054 forcing marine air intrusions into West Antarctica, *Clim. Dyn.*, 1–18, doi:10.1007/s00382-018-
 1055 4097-3, 2018.
- 1056 EPICA Community Members: One-to-one coupling of glacial climate variability in Greenland
 1057 and Antarctica., *Nature*, 444, 195–198, doi:10.1038/nature05301, 2006.
- 1058 Frezzotti, M., Urbini, S., Proposito, M., Sarchilli, C. and Gandolfi, S.: Spatial and temporal
 1059 variability of surface mass balance near Talos Dome, East Antarctica, *J. Geophys. Res. Earth
 1060 Surf.*, 112(2), doi:10.1029/2006JF000638, 2007.
- 1061 Frezzotti, M., Sarchilli, C., Becagli, S., Proposito, M. and Urbini, S.: A synthesis of the
 1062 Antarctic surface mass balance during the last 800 yr, *Cryosphere*, 7(1), 303–319,
 1063 doi:10.5194/tc-7-303-2013, 2013.
- 1064 Friß, U., Deutschmann, T., Gilfedder, B., Weller, R. and Platt, U.: Iodine monoxide in the
 1065 Antarctic snowpack, *Atmos. Chem. Phys.*, 2439–2456, doi:10.5194/acp-10-2439-2010, 2010.

- 1066 Fudge, T. J., Markle, B. R., Cuffey, K. M., Buizert, C., Taylor, K. C., Steig, E. J., Waddington,
1067 E. D., Conway, H. and Koutnik, M.: Variable relationship between accumulation and
1068 temperature in West Antarctica for the past 31,000 years, *Geophys. Res. Lett.*, 3795–3803,
1069 doi:10.1002/2016GL068356, 2016.
- 1070 Gabrieli, J., Cozzi, G., Vallelonga, P., Schwikowski, M., Sigl, M., Eickenberg, J., Wacker, L.,
1071 Boutron, C., Gäggeler, H., Cescon, P. and Barbante, C.: Contamination of Alpine snow and ice
1072 at Colle Gnifetti, Swiss/Italian Alps, from nuclear weapons tests, *Atmos. Environ.*, 45(3), 587–
1073 593, doi:10.1016/j.atmosenv.2010.10.039, 2011.
- 1074 Hammer, C.: Acidity of polar ice cores in relation to absolute dating, past volcanism, and radio-
1075 echoes, *J. Glaciol.*, 25, 359–372, doi:10.3189/S0022143000015227, 1980.
- 1076 Hammer, C. ., Clausen, H. B., Dansgaard, W., Gundestrup, N., Johnsen, S. and Reeh, N.: Dating
1077 of Greenland ice cores by flow models, isotopes, volcanic debris, and continental dust, *J.*
1078 *Glaciol.*, 20(82), 3–26, doi:10.3189/S0022143000021183, 1978.
- 1079 Haran, T., Bohlander, J., Scambos, T., Painter, T. and Fahnestock, M.: MODIS Mosaic of
1080 Antarctica 2003-2004 (MOA2004) Image Map, National Snow and Ice Data Center, Boulder,
1081 Colorado, USA, 2013.
- 1082 Herron, M. M. and Langway, C. C.: Dating of Ross Ice Shelf Cores by Chemical Analysis, *J.*
1083 *Glaciol.*, 24(90), 345–356, doi:10.3189/S0022143000014866, 1979.
- 1084 Herron, M. M. and Langway, C. C.: Firn densification: an empirical model, *J. Glaciol.*, 25(93),
1085 373–385, doi:10.3189/S0022143000015239, 1980.
- 1086 Hosking, J. S., Orr, A., Marshall, G. J., Turner, J. and Phillips, T.: The influence of the
1087 amundsen-bellingshausen seas low on the climate of West Antarctica and its representation in
1088 coupled climate model simulations, *J. Clim.*, 26(17), 6633–6648, doi:10.1175/JCLI-D-12-
1089 00813.1, 2013.
- 1090 Jiracek, G. R.: Radio sounding of Antarctic ice, *Univ. Wisconsin Res. Rep.*, 67(1), 1967.
- 1091 Jones, J. M., Gille, S. ., Goosse, H., Abram, N. J., Canziani, P., Charman, D., Clem, K., Crosta,
1092 X., Lavergne, C. de, Eisenman, G., England, M. H., Fogt, R., Frankcombe, L. M., Marshall, G.,
1093 Masson-delmotte, V., Morrison, A. K., Orsi, A., Raphael, M. N., Renwick, J. A., Schneider, D.
1094 P., Simpkins, G. R., Steig, E. J., Stenni, B., Swingedouw, D. and Vance, T. R.: Assessing recent
1095 trends in high-latitude Southern Hemisphere surface climate, *Nat. Clim. Chang.*, 6, 917–926,
1096 doi:10.1038/nclimate3103, 2016.
- 1097 Kaspari, S., Mayewski, P. A., Dixon, D. A., Spikes, V. B., Sneed, S. B., Handley, M. J. and
1098 Hamilton, G. S.: Climate variability in West Antarctica derived from annual accumulation-rate
1099 records from ITASE firn/ice cores, *Ann. Glaciol.*, 39, 585–594,
1100 doi:10.3189/172756404781814447, 2004.
- 1101 Keller, E. D., Baisden, W. T., Bertler, N. A. N., Emanuelsson, B. D., Canessa, S. and Phillips,
1102 A.: Calculating uncertainty for the RICE ice core continuous flow analysis water isotope record,
1103 *Atmos. Meas. Tech. Discuss.*, 2018, 1–20, doi:10.5194/amt-2017-387, 2018.
- 1104 Kingslake, J., Hindmarsh, R. C. A., Adalgeirsdottir, G., Conway, H., Pritchard, H. D., Corr, H.
1105 F. J., Gillet-Chaulet, F., Martin, C., King, E. C., Mulvaney, R. and Pritchard, H. D.: Full-depth
1106 englacial vertical ice sheet velocities measured using phase-sensitive radar, *J. Geophys. Res.*
1107 *Earth Surf.*, 119, 2604–1618, doi:10.1002/2014JF003275, 2014.

- 1108 Kjær, H. A., Vallelonga, P., Svensson, A., Elleskov Kristensen, M. L., Tibuleac, C., Winstrup,
1109 M. and Kipfstuhl, S.: An Optical Dye Method for Continuous Determination of Acidity in Ice
1110 Cores, *Environ. Sci. Technol.*, 50(19), 10485–10493, doi:10.1021/acs.est.6b00026, 2016.
- 1111 Kurbatov, A. V., Kalteyer, D. A., Dunbar, N. W., Yates, M. G., Iverson, N. A. and Bertler, N.
1112 A.: Major element analyses of visible tephra layers in the Roosevelt Island Climate Evolution
1113 Project ice core (Antarctica), *Interdiscip. Earth Data Alliance*, doi:10.1594/IEDA/100554,
1114 2015.
- 1115 Kushner, P. J., Held, I. M. and Delworth, T. L.: Southern Hemisphere Atmospheric Circulation
1116 Response to Global Warming, *J. Clim.*, 14(10), 2238–2249, doi:10.1175/1520-
1117 0442(2001)014<0001:SHACRT>2.0.CO;2, 2001.
- 1118 Kuttel, M., Steig, E. J., Ding, Q., Monaghan, A. J. and Battisti, D. S.: Seasonal climate
1119 information preserved in West Antarctic ice core water isotopes : relationships to temperature,
1120 large-scale circulation, and sea ice, *Clim. Dyn.*, 39, 1841–1857, doi:10.1007/s00382-012-1460-
1121 7, 2012.
- 1122 Lamarque, J. F., Bond, T. C., Eyring, V., Granier, C., Heil, A., Klimont, Z., Lee, D., Liousse,
1123 C., Mieville, A., Owen, B., Schultz, M. G., Shindell, D., Smith, S. J., Stehfest, E., Van
1124 Aardenne, J., Cooper, O. R., Kainuma, M., Mahowald, N., McConnell, J. R., Naik, V., Riahi,
1125 K. and Van Vuuren, D. P.: Historical (1850-2000) gridded anthropogenic and biomass burning
1126 emissions of reactive gases and aerosols: Methodology and application, *Atmos. Chem. Phys.*,
1127 10(15), 7017–7039, doi:10.5194/acp-10-7017-2010, 2010.
- 1128 Langway, C. C., Herron, M. and Cragin, J. H.: Chemical Profile of the Ross Ice Shelf at Little
1129 America V, *Antarctica, J. Glaciol.*, 13(69), 431–435, doi:10.3189/S0022143000023200, 1974.
- 1130 Lee, J., Brook, E. J., Bertler, N. A. N., Buizert, C., Baisden, W. T., Blunier, T., Ciobanu, G.,
1131 Conway, H., Dahl-Jensen, D., Fudge, T. J., Hindmarsh, R. C. A., Keller, E. D., Parrenin, F.,
1132 Severinghaus, J. P., Vallelonga, P., Waddington, E. D. and Winstrup, M.: A 83,000 year old ice
1133 core from Roosevelt Island, Ross Sea, Antarctica, *Clim. Past Discuss.*, 1–44, doi:10.5194/cp-
1134 2018-68, 2018.
- 1135 Legrand, M., Feniet-Saigne, C., Saltzman, E. S., Germain, C., Barkov, N. I. and Petrov, V. N.:
1136 Ice-core record of oceanic emissions of dimethylsulphide during the last climate cycle, *Nature*,
1137 350(6314), 144–146, doi:10.1038/350144a0, 1991.
- 1138 Lliboutry, L. A.: A critical review of analytical approximate solutions for steady state velocities
1139 and temperatures in cold ice sheets, *Gletscherkd. Glazialgeol*, 15(2), 135–148, 1979.
- 1140 Marshall, G. J.: Trends in the Southern Annular Mode from Observations and Reanalyses, *J.*
1141 *Clim.*, 16(24), 4134–4143, doi:10.1175/1520-0442(2003)016<4134:TITSAM>2.0.CO;2,
1142 2003.
- 1143 Martín, C., Hindmarsh, R. C. A. and Navarro, F. J.: Dating ice flow change near the flow divide
1144 at Roosevelt Island, Antarctica, by using a thermomechanical model to predict radar
1145 stratigraphy, *J. Geophys. Res. Earth Surf.*, 111(1), 1–15, doi:10.1029/2005JF000326, 2006.
- 1146 McConnell, J. R., Edwards, R., Kok, G. L., Flanner, M. G. and Zender, C. S.: 20th-Century
1147 industrial black carbon emissions altered Arctic climate forcing, *Science*, 317(5843), 1381–
1148 1384, doi:10.1126/science.1144856, 2007.

- 1149 Mitchell, L. E., Brook, E. J., Sowers, T., McConnell, J. R. and Taylor, K.: Multidecadal
 1150 variability of atmospheric methane, 1000-1800 C.E., *J. Geophys. Res. Biogeosciences*, 116(2),
 1151 1–16, doi:10.1029/2010JG001441, 2011.
- 1152 Mitchell, L. E., Brook, E. J., Lee, J. E., Buizert, C. and Sowers, T.: Constraints on the Late
 1153 Holocene Anthropogenic Contribution to the Atmospheric Methane Budget, *Science*,
 1154 342(6161), 964–966, doi:10.1126/science.1238920, 2013.
- 1155 Mudelsee, M.: Break function regression, *Eur. Phys. J. Spec. Top.*, 174(1), 49–63,
 1156 doi:10.1140/epjst/e2009-01089-3, 2009.
- 1157 Muscheler, R., Adolphi, F. and Knudsen, M. F.: Assessing the differences between the IntCal
 1158 and Greenland ice-core time scales for the last 14,000 years via the common cosmogenic
 1159 radionuclide variations, *Quat. Sci. Rev.*, 106, 81–87, doi:10.1016/j.quascirev.2014.08.017,
 1160 2014.
- 1161 Narcisi, B., Proposito, M. and Frezzotti, M.: Ice record of a 13th century explosive volcanic
 1162 eruption in northern Victoria Land, East Antarctica, *Antarct. Sci.*, 13(2), 174–181,
 1163 doi:10.1017/S0954102001000268, 2001.
- 1164 Narcisi, B., Petit, J. R., Delmonte, B., Scarchilli, C. and Stenni, B.: A 16,000-yr tephra
 1165 framework for the Antarctic ice sheet: A contribution from the new Talos Dome core, *Quat.*
 1166 *Sci. Rev.*, 49, 52–63, doi:10.1016/j.quascirev.2012.06.011, 2012.
- 1167 Nereson, N. A. and Waddington, E. D.: Isochrones and isotherms beneath migrating ice divides,
 1168 *J. Glaciol.*, 48(160), 95–108, doi:10.3189/172756502781831647, 2002.
- 1169 Noone, D. and Simmons, I.: Sea ice control of water isotope transport to Antarctica and
 1170 implications for ice core interpretation, *J. Geophys. Res.*, 109, 1–13,
 1171 doi:10.1029/2003JD004228, 2004.
- 1172 Nye, J. F.: Correction Factor for Accumulation Measured by the Thickness of the Annual
 1173 Layers in an Ice Sheet, *J. Glaciol.*, 4(36), 785–788, doi:10.3189/S0022143000028367, 1963.
- 1174 Philippe, M., Tison, J. L., Fjøsne, K., Hubbard, B., Kjær, H. A., Lenaerts, J. T. M., Drews, R.,
 1175 Sheldon, S. G., De Bondt, K., Claeys, P. and Pattyn, F.: Ice core evidence for a 20th century
 1176 increase in surface mass balance in coastal Dronning Maud Land, East Antarctica, *Cryosph.*,
 1177 10(5), 2501–2516, doi:10.5194/tc-10-2501-2016, 2016.
- 1178 Rabiner, L. R.: A Tutorial on Hidden Markov Models and Selected Applications in Speech
 1179 Recognition, *Proc. IEEE*, 77(2), 257–286, doi:10.1109/5.18626, 1989.
- 1180 Raisbeck, G. M., Cauquoin, A., Jouzel, J., Landais, A., Petit, J.-R., Lipenkov, V. Y., Beer, J.,
 1181 Synal, H.-A., Oerter, H., Johnsen, S. J., Steffensen, J. P., Svensson, A. and Yiou, F.: An
 1182 improved north–south synchronization of ice core records around the 41 kyr ¹⁰Be peak, *Clim.*
 1183 *Past*, 13(3), 217–229, doi:10.5194/cp-13-217-2017, 2017.
- 1184 Raphael, M. N., Marshall, G. J., Turner, J., Fogt, R. L., Schneider, D., Dixon, D. A., Hosking,
 1185 J. S., Jones, J. M. and Hobbs, W. R.: The Amundsen sea low: Variability, change, and impact
 1186 on Antarctic climate, *Bull. Am. Meteorol. Soc.*, 97(1), 111–121, doi:10.1175/BAMS-D-14-
 1187 00018.1, 2016.
- 1188 Rasmussen, S. O., Andersen, K. K., Svensson, A. M., Steffensen, J. P., Vinther, B. M., Clausen,
 1189 H. B., Siggaard-Andersen, M. L., Johnsen, S. J., Larsen, L. B., Dahl-Jensen, D., Bigler, M.,
 1190 Röthlisberger, R., Fischer, H., Goto-Azuma, K., Hansson, M. E. and Ruth, U.: A new Greenland

- 1191 ice core chronology for the last glacial termination, *J. Geophys. Res. Atmos.*, 111(6),
1192 doi:10.1029/2005JD006079, 2006.
- 1193 Raymond, C. F.: Deformation in the Vicinity of Ice Divides, *J. Glaciol.*, 29(103), 357–373,
1194 doi:10.3189/S0022143000030288, 1983.
- 1195 Schultz, M. G., Heil, A., Hoelzemann, J. J., Spessa, A., Thonicke, K., Goldammer, J. G., Held,
1196 A. C., Pereira, J. M. C. and van Het Bolscher, M.: Global wildland fire emissions from 1960 to
1197 2000, *Global Biogeochem. Cycles*, 22(2), 1–17, doi:10.1029/2007GB003031, 2008.
- 1198 Schwander, J. and Stauffer, B.: Age difference between polar ice and the air trapped in its
1199 bubbles, *Nature*, 311, 45–47, doi:10.1038/311045a0, 1984.
- 1200 Shepherd, A., Ivins, E. R., A, G., Barletta, V. R., Bentley, M. J., Bettadpur, S., Briggs, K. H.,
1201 Bromwich, D. H., Forsberg, R., Galin, N., Horwath, M., Jacobs, S., Joughin, I., King, M. A.,
1202 Lenaerts, J. T., Li, J., Ligtenberg, S. R. M., Luckman, A., McMillan, M., Meister, R., Milne,
1203 G., Mouginot, J., Muir, A., Nicolas, J., Paden, J., Payne, A. J., Pritchard, H. D., Rignot, E., Rott,
1204 H., Sørensen, L. S., Scambos, T. A., Scheuchl, B., Schrama, E. J. O., Smith, B., Sundal, A. V.,
1205 Angelen, J. H. van, Berg, W. J. van der, Broeke, M. R. van der, Vaughan, D. G., Velicogna, I.,
1206 Wahr, J., Whitehouse, P. L., Wingham, D. J., Yi, D., Young, D. and Zwally, H. J.: A Reconciled
1207 Estimate of Ice-Sheet Mass Balance, *Science*, 338, 1183–1190, doi:10.1126/science.1228102,
1208 2012.
- 1209 Sigl, M., McConnell, J. R., Layman, L., Maselli, O., McGwire, K., Pasteris, D., Dahl-Jensen,
1210 D., Steffensen, J. P., Vinther, B., Edwards, R., Mulvaney, R. and Kipfstuhl, S.: A new bipolar
1211 ice core record of volcanism from WAIS Divide and NEEM and implications for climate
1212 forcing of the last 2000 years, *J. Geophys. Res. Atmos.*, 118(3), 1151–1169,
1213 doi:10.1029/2012JD018603, 2013.
- 1214 Sigl, M., Winstrup, M., McConnell, J. R., Welten, K. C., Plunkett, G., Ludlow, F., Büntgen, U.,
1215 Caffee, M., Chellman, N., Dahl-Jensen, D., Fischer, H., Kipfstuhl, S., Kostick, C., Maselli, O.
1216 J., Mekhaldi, F., Mulvaney, R., Muscheler, R., Pasteris, D. R., Pilcher, J. R., Salzer, M.,
1217 Schüpbach, S., Steffensen, J. P., Vinther, B. M. and Woodruff, T. E.: Timing and climate
1218 forcing of volcanic eruptions for the past 2,500 years., *Nature*, 523(7562), 543–9,
1219 doi:10.1038/nature14565, 2015.
- 1220 Sigl, M., Fudge, T. J., Winstrup, M., Cole-Dai, J., Ferris, D., McConnell, J. R., Taylor, K. C.,
1221 Welten, K. C., Woodruff, T. E., Adolphi, F., Bisiaux, M., Brook, E. J., Buizert, C., Caffee, M.
1222 W., Dunbar, N. W., Edwards, R., Geng, L., Iverson, N., Koffman, B., Layman, L., Maselli, O.
1223 J., McGwire, K., Muscheler, R., Nishiizumi, K., Pasteris, D. R., Rhodes, R. H. and Sowers, T.
1224 A.: The WAIS Divide deep ice core WD2014 chronology - Part 2: Annual-layer counting (0-
1225 31 ka BP), *Clim. Past*, 12(3), 769–786, doi:10.5194/cp-12-769-2016, 2016.
- 1226 Spolaor, A., Vallelonga, P., Gabrieli, J., Martma, T., Björkman, M. P., Isaksson, E., Cozzi, G.,
1227 Turetta, C., Kjær, H. A., Curran, M. A. J., Moy, A. D., Schönhardt, A., Blechschmidt, A. M.,
1228 Burrows, J. P., Plane, J. M. C. and Barbante, C.: Seasonality of halogen deposition in polar
1229 snow and ice, *Atmos. Chem. Phys.*, 14(18), 9613–9622, doi:10.5194/acp-14-9613-2014, 2014.
- 1230 Steig, E. J., Mayewski, P. A., Dixon, D. A., Kaspari, S. D., Frey, M. M., Schneider, D. P.,
1231 Arcone, S. A., Hamilton, G. S., Spikes, V. B., Albert, M., Meese, D., Gow, A. J., Shuman, C.
1232 A., White, J. W. C., Sneed, S., Flaherty, J. and Wumkes, M.: High-resolution ice cores from
1233 US ITASE (West Antarctica): development and validation of chronologies and determination
1234 of precision and accuracy, *Ann. Glaciol.*, 41(1), 77–84, doi:10.3189/172756405781813311,
1235 2005.

- 1236 Stenni, B., Proposito, M., Gragnani, R., Flora, O., Jouzel, J., Falourd, S. and Frezzotti, M.: Eight
 1237 centuries of volcanic signal and climate change at Talos Dome (East Antarctica), *J. Geophys.*
 1238 *Res.*, 107(D9), 1–13, doi:10.1029/2000JD000317, 2002.
- 1239 Stenni, B., Curran, M. A. J., Abram, N. J., Orsi, A., Goursaud, S., Masson-Delmotte, V.,
 1240 Neukom, R., Goosse, H., Divine, D., van Ommen, T., Steig, E. J., Dixon, D. A., Thomas, E. R.,
 1241 Bertler, N. A. N., Isaksson, E., Ekaykin, A., Frezzotti, M. and Werner, M.: Antarctic climate
 1242 variability at regional and continental scales over the last 2000 years, *Clim. Past*, 13, 1609–
 1243 1634, doi:10.5194/cp-2017-40, 2017.
- 1244 Stowasser, C., Buizert, C., Gkinis, V., Chappellaz, J., Schapbach, S., Bigler, M., Fan, X.,
 1245 Sperlich, P., Baumgartner, M., Schilt, A. and Blunier, T.: Continuous measurements of methane
 1246 mixing ratios from ice cores, *Atmos. Meas. Tech.*, 5(5), 999–1013, doi:10.5194/amt-5-999-
 1247 2012, 2012.
- 1248 Svensson, A., Andersen, K. K., Bigler, M., Clausen, H. B., Dahl-Jensen, D., Davies, S. M.,
 1249 Johnsen, S. J., Muscheler, R., Parrenin, F., Rasmussen, S. O., Rothlisberger, R., Seierstad, I.,
 1250 Steffensen, J. P. and Vinther, B. M.: A 60 000 year Greenland stratigraphic ice core chronology,
 1251 *Clim. Past*, 4, 47–57, doi:10.5194/cpd-3-1235-2007, 2008.
- 1252 Svensson, A., Bigler, M., Blunier, T., Clausen, H. B., Dahl-Jensen, D., Fischer, H., Fujita, S.,
 1253 Goto-Azuma, K., Johnsen, S. J., Kawamura, K., Kipfstuhl, S., Kohno, M., Parrenin, F., Popp,
 1254 T., Rasmussen, S. O., Schwander, J., Seierstad, I., Severi, M., Steffensen, J. P., Udisti, R.,
 1255 Uemura, R., Vallelonga, P., Vinther, B. M., Wegner, A., Wilhelms, F. and Winstrup, M.: Direct
 1256 linking of Greenland and Antarctic ice cores at the Toba eruption (74 ka BP), *Clim. Past*, 9(2),
 1257 749–766, doi:10.5194/cp-9-749-2013, 2013.
- 1258 Thomas, E. R. and Abram, N. J.: Ice core reconstruction of sea ice change in the Amundsen-
 1259 Ross Seas since 1702 A.D., *Geophys. Res. Lett.*, 43(10), 5309–5317,
 1260 doi:10.1002/2016GL068130, 2016.
- 1261 Thomas, E. R., Hosking, J. S., Tuckwell, R. R., Warren, R. A. and Ludlow, E. C.: Twentieth
 1262 century increase in snowfall in coastal West Antarctica, *Geophys. Res. Lett.*, 42(21), 9387–
 1263 9393, doi:10.1002/2015GL065750, 2015.
- 1264 Thomas, E. R., van Wessel, J. M., Roberts, J., Isaksson, E., Schlosser, E., Fudge, T.,
 1265 Vallelonga, P., Medley, B., Lenaerts, J., Bertler, N., van den Broeke, M. R., Dixon, D. A.,
 1266 Frezzotti, M., Stenni, B., Curran, M. and Ekaykin, A. A.: Regional Antarctic snow
 1267 accumulation over the past 1000 years, *Clim. Past*, 13, 1491–1513, doi:10.5194/cp-13-1491-
 1268 2017, 2017.
- 1269 Traversi, R., Becagli, S., Castellano, E., Maggi, V., Morganti, A., Severi, M. and Udisti, R.:
 1270 Ultra-sensitive Flow Injection Analysis (FIA) determination of calcium in ice cores at ppt level,
 1271 *Anal. Chim. Acta*, 594(2), 219–225, doi:10.1016/j.aca.2007.05.022, 2007.
- 1272 Tuohy, A., Bertler, N., Neff, P., Edwards, R., Emanuelsson, D., Beers, T. and Mayewski, P.:
 1273 Transport and deposition of heavy metals in the Ross Sea Region, Antarctica, *J. Geophys. Res.*
 1274 *Atmos.*, 120(20), 10996–11011, doi:10.1002/2015JD023293, 2015.
- 1275 Turner, J., Comiso, J. C., Marshall, G. J., Lachlan-cope, T. A., Bracegirdle, T., Maksym, T.,
 1276 Meredith, M. P., Wang, Z. and Orr, A.: Non-annular atmospheric circulation change induced
 1277 by stratospheric ozone depletion and its role in the recent increase of Antarctic sea ice extent,
 1278 *Geophys. Res. Lett.*, 36(L08502), 1–5, doi:10.1029/2009GL037524, 2009.

1279 Turner, J., Hosking, J. S., Marshall, G. J., Phillips, T. and Bracegirdle, T. J.: Antarctic sea ice
1280 increase consistent with intrinsic variability of the Amundsen Sea Low, *Clim. Dyn.*, 46(7),
1281 2391–2402, doi:10.1007/s00382-015-2708-9, 2016.

1282 Udisti, R., Traversi, R., Becagli, S. and Piccardi, G.: Spatial distribution and seasonal pattern
1283 of biogenic sulphur compounds in snow from northern Victoria Land, Antarctica, *Ann. Glaciol.*,
1284 27, 535–542, doi:10.3189/1998AoG27-1-535-542, 1998.

1285 WAIS Divide Project Members: Precise inter-polar phasing of abrupt climate change during the
1286 last ice age, *Nature*, 520(7549), 661–665, doi:10.1038/nature14401, 2015.

1287 Wheatley, S. and Kurbatov, A. V.: Antarctic Ice Core Tephra Analysis, U.S. Antarct. Progr.
1288 Data Center. Dataset., doi:10.15784/601038, 2017.

1289 Winstrup, M.: A Hidden Markov Model Approach to Infer Timescales for High-Resolution
1290 Climate Archives, in Proceedings of the 30th AAAI Conference on Artificial Intelligence and
1291 the 28th Innovative Applications of Artificial Intelligence Conference, pp. 4053–4061, AAAI
1292 Press, Palo Alto, California, February 12 – 17, 2016, Phoenix, Arizona USA., 2016.

1293 Winstrup, M., Svensson, A. M., Rasmussen, S. O., Winther, O., Steig, E. J. and Axelrod, A. E.:
1294 An automated approach for annual layer counting in ice cores, *Clim. Past*, 8(6), 1881–1895,
1295 doi:10.5194/cp-8-1881-2012, 2012.

1296 Yu, S. Z.: Hidden semi-Markov models, *Artif. Intell.*, 174(2), 215–243,
1297 doi:10.1016/j.artint.2009.11.011, 2010.

1298 Yuan, X. and Martinson, D. G.: Antarctic sea ice extent variability and its global connectivity,
1299 *J. Clim.*, 13(10), 1697–1717, doi:10.1175/1520-0442(2000)013<1697:ASIEVA>2.0.CO;2,
1300 2000.

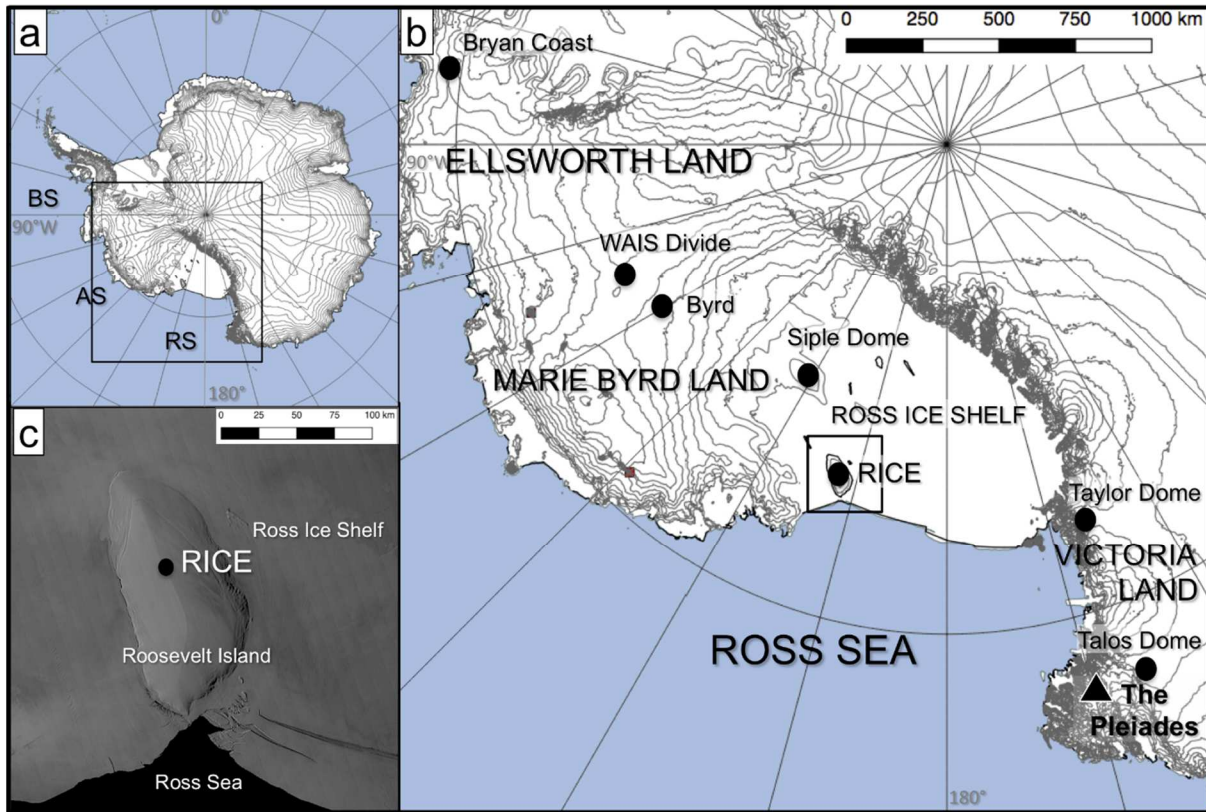
1301 Zreda-Gostynska, G., Kyle, P. R., Finnegan, D. and Meeker Prestbo, K.: Volcanic gas
1302 emissions from Mount Erebus and their impact on the Antarctic environment, *J. Geophys. Res.*,
1303 102055(10), 39–15, doi:10.1029/97JB00155, 1997.

1304

1305

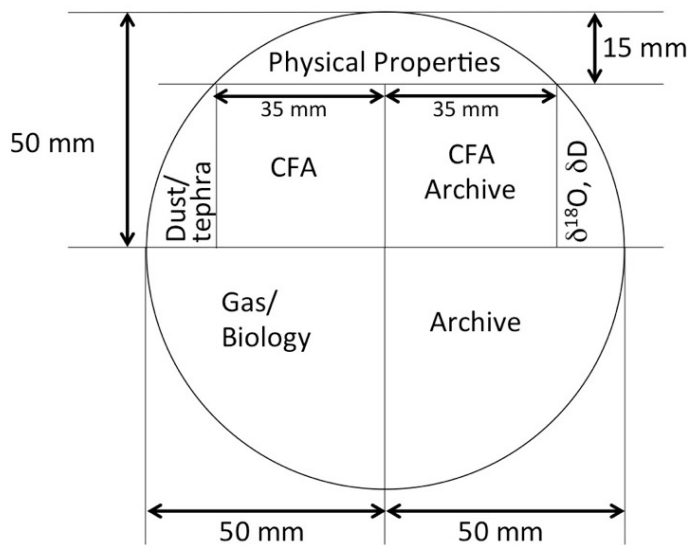
1306

1307



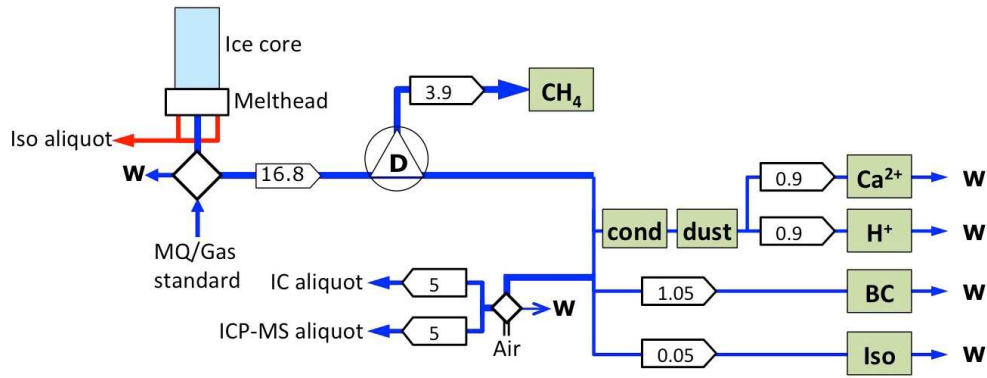
1309
1310

1311 **Figure 1: a, b):** Roosevelt Island is located in the eastern sector of the Ross Ice Shelf
 1312 embayment. Locations discussed in the text are represented by circles (ice cores) and triangle
 1313 (volcano). RS: Ross Sea; AS: Amundsen Sea; BS: Bellingshausen Sea. **c)** MODIS image of
 1314 Roosevelt Island (Haran et al. 2013), protruding as an ice dome from the surrounding Ross Ice
 1315 Shelf. The RICE ice core was drilled on the ice divide of Roosevelt Island.



1316

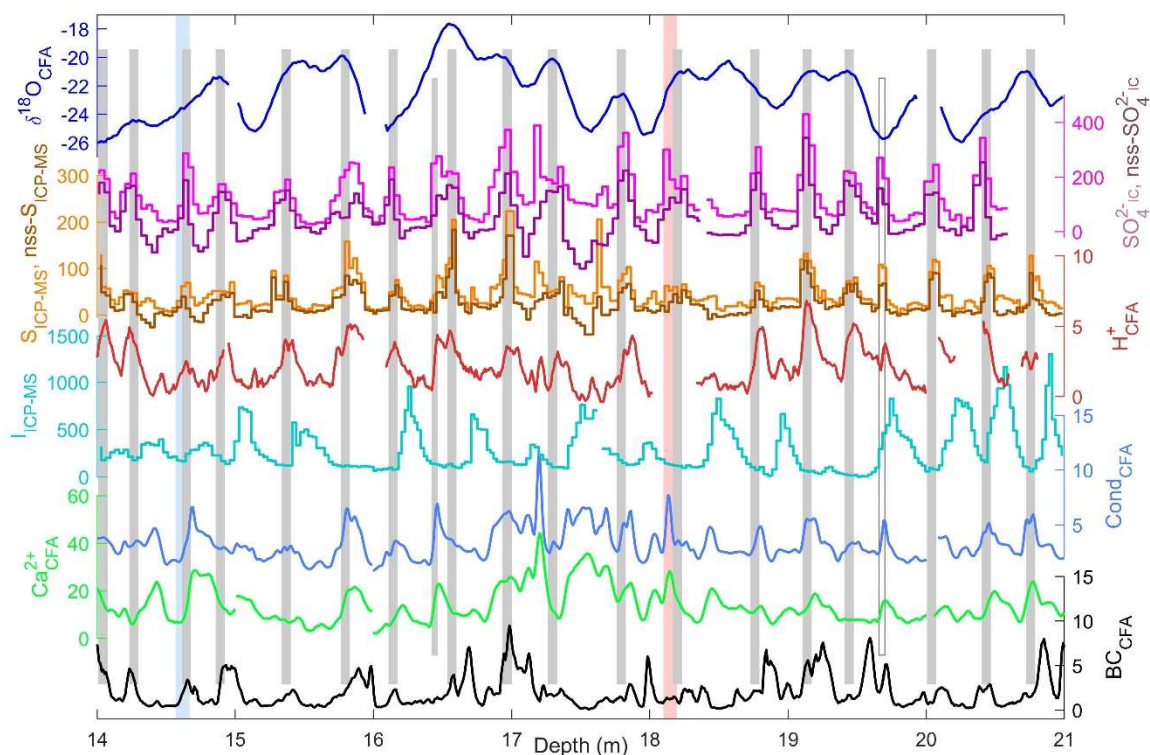
1317 **Figure 2:** The RICE main core cutting plan included 2 CFA sticks of size 35x35mm.



1318

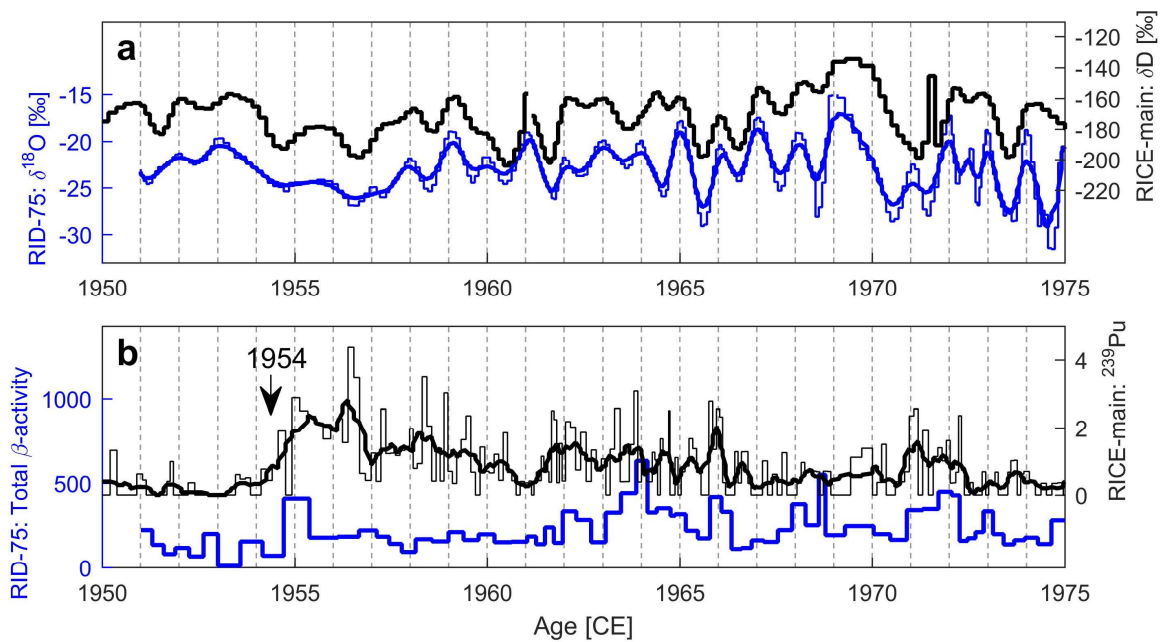
1319 **Figure 3:** The RICE CFA set-up. A 1 m long ice-core rod (light blue) is placed on a melt head,
 1320 which separates melt water from the pristine inner part of the core from that of the more
 1321 contaminated outer rim. Meltwater from the outer stream (red) is used for discrete
 1322 measurements of water isotopes, while the melt water stream from the inner core section (dark
 1323 blue) passes through a debubbler (D), which separates air from the melt water. The air
 1324 composition is analyzed for methane concentration, while the meltwater stream is channeled to
 1325 various analytical instruments for continuous impurity analysis of dust, conductivity (cond),
 1326 calcium (Ca²⁺), acidity (H⁺), black carbon (BC), and water isotopes (Iso), as well as collected
 1327 in vials for discrete aliquot sampling by IC and ICP-MS. W denotes waste water. Diamonds
 1328 represent injection valves used for introduction of air or water standards when the melter system
 1329 is not in use. Arrow boxes indicate liquid flow rates in mL min⁻¹. Green boxes represent
 1330 analytical instruments.

1331



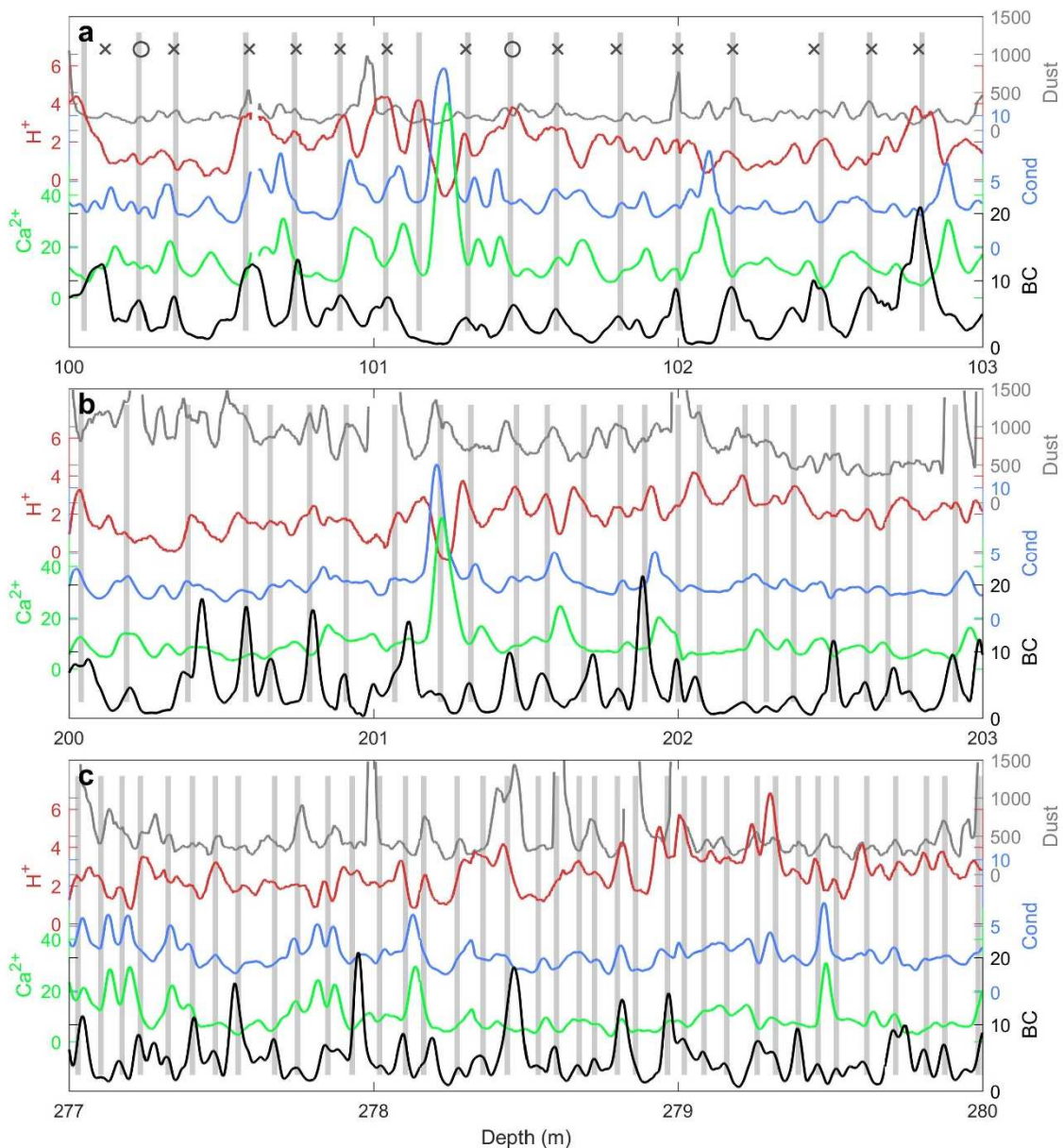
1332

1333 **Figure 4:** Assignment of annual layers in an upper section of the RICE core. All units are in
 1334 ppb, except for $\delta^{18}\text{O}$ (in ‰), H^+ (in $\mu\text{eq L}^{-1}$), and conductivity (in $\mu\text{S cm}^{-1}$). The CFA chemistry
 1335 records are smoothed with a 3-cm moving average filter. The timescale is constrained by two
 1336 tie-points within this interval: the isotope match to RID-75 (blue bar; 14.6 m) and the Raoul
 1337 tephra horizon (red bar; 18.1 m). At two locations, the annual layering is unclear (shorter bars),
 1338 but can be mostly resolved on basis of the tie-point ages. As a result, the uncertain layer at 16.6 m
 1339 (short grey bar) is included as a year in the timescale, whereas the uncertain layer at 19.7m
 1340 (short white bar) is not. For the second layer, the sulfate record suggests that it is an annual
 1341 layer, but this is not supported by iodine and $\delta^{18}\text{O}$. As we assume an uncertainty of ± 1 yr for the
 1342 tie-point ages, the layer at 16.6m could possibly be removed from the timescale, while still
 1343 adhering to the age constraints. The existence of this uncertain layer therefore gives rise to a 1-
 1344 year increase of the timescale uncertainty.



1345

1346 **Figure 5:** a) RICE water isotope profile (δD) compared to isotope data ($\delta^{18}\text{O}$) from the RID-
 1347 75 core for the period 1950-1975. Diffusion causes the isotope record to smooth over time, and
 1348 a smoothed version of the RID-75 isotope profile (thick blue) highlights its similarities to the
 1349 RICE isotope record (black). b) Total specific β -activity (in disintegrations per hour, dph)
 1350 for the RID-75 core compared to ^{239}Pu measurements (normalized intensities) from the RICE main
 1351 core. Both cores show a sharp increase in nuclear waste deposition starting in 1954 CE, and
 1352 several broader peaks hereafter.

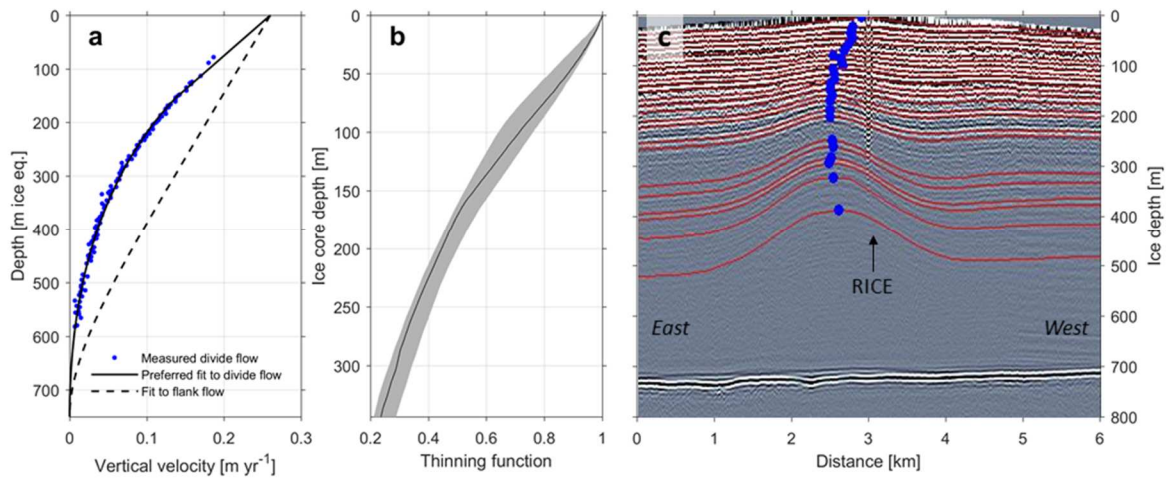


1353

1354 **Figure 6:** CFA data and annual layer counts (grey bars) in three 3m-long sections (a-c) of the
 1355 RICE core. In general, the most distinct annual signal is found in the BC record, but the other
 1356 records also contain valuable information on the annual layering. Due to contamination from
 1357 drill fluid, the dust record was not used for layer counting below 129m. For the top section (a),
 1358 the preliminary set of manual layer counts used for initializing StratiCounter are shown: Crosses
 1359 (x) indicate certain layers and circles (o) indicate uncertain layers. For this section, the manual
 1360 layer counts have a bias towards counting too few layers in total. This is a general tendency of
 1361 the manual timescale, resulting in a manually-counted age for the Pleiades tephra that is a few
 1362 decades younger than observed in WAIS Divide.

1363

1364



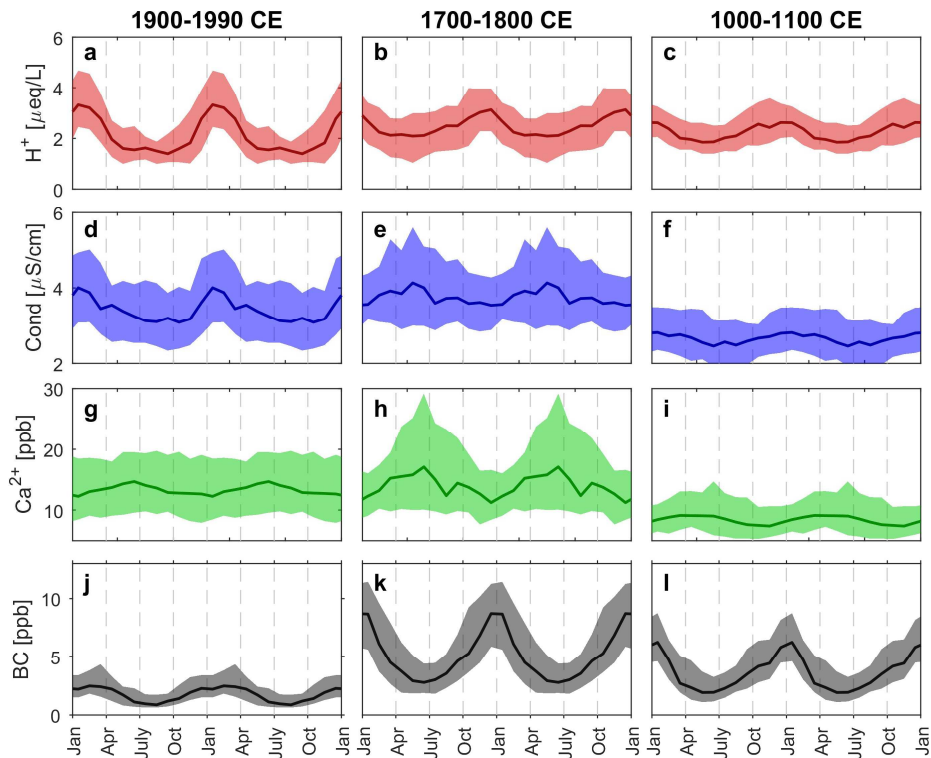
1365
1366

1367 **Figure 7: a)** Vertical velocity profiles for divide-like flow and flank flow (Kingslake et al.,
1368 2014). For divide flow is plotted the preferred Lliboutry-fit along with the measured vertical
1369 velocities (blue dots). **b)** Thinning function with associated 95% confidence interval. **c)** Radar
1370 echogram (Kingslake et al., 2014) with traced layers (red) and location of maximum amplitudes
1371 of the stack of Raymond arches (blue circles). The location of the modern topographic ice divide
1372 (and the RICE drill site) is marked by the returns from a pole. The core site is located west of
1373 the maximum bump amplitudes at depth.

1374

1375

1376



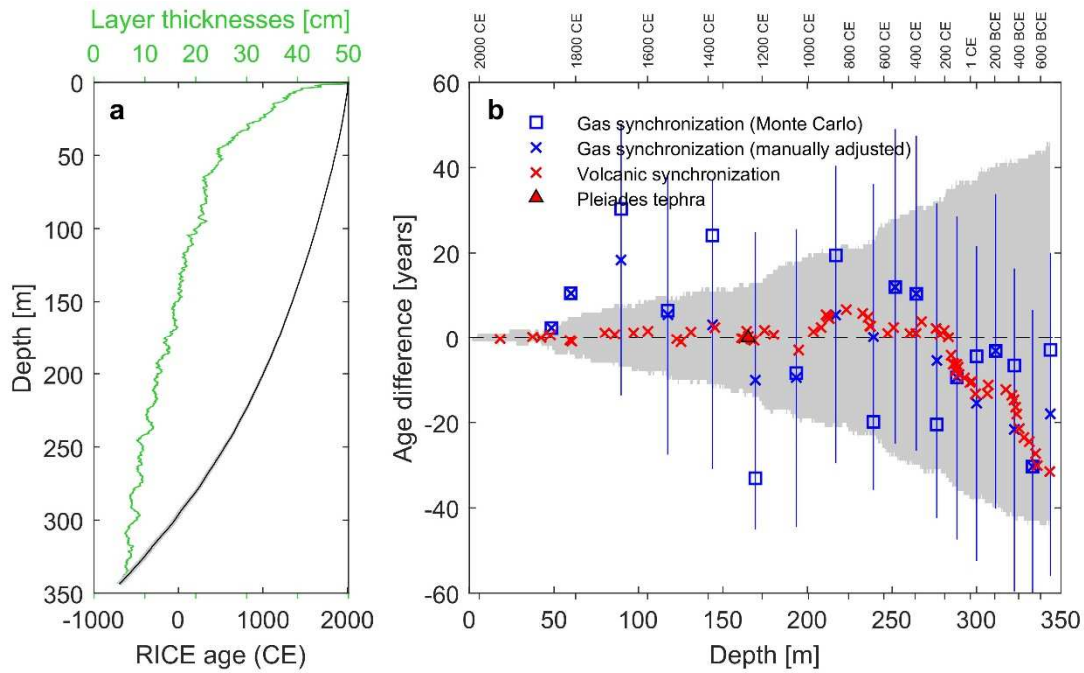
1377

1378 **Figure 8:** Average annual signals of 2 successive years in **a-c)** acidity (H^+), **d-f)** conductivity
1379 (Cond), **g-i)** calcium (Ca^{2+}), and **j-l)** black carbon (BC) during three centuries, calculated under
1380 the assumption of constant snowfall through the year. The main RICE CFA data only extends
1381 to 1990 CE. The line shows the monthly-averaged median value of measured concentrations,
1382 and colored area signifies the 50% quantile envelope of the value distribution.

1383

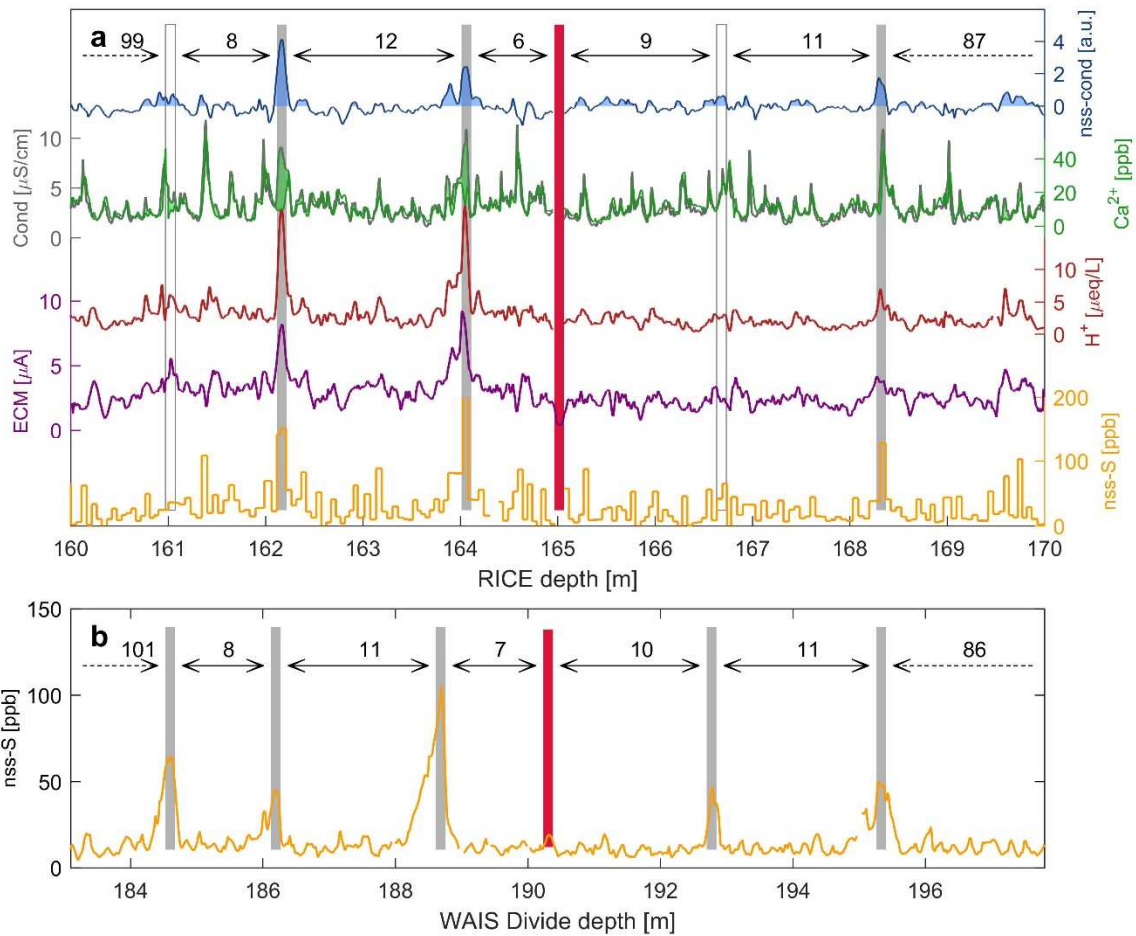
1384

1385



1386

1387 **Figure 9:** a) Depth evolution of RICE17 ages (black), including the associated 95% confidence
1388 interval (grey area, almost invisible due to scale), and corresponding mean layer thicknesses
1389 (50 year running mean; green). b) Comparison of RICE17 ages and confidence interval (grey
1390 area) to WD2014 from volcanic (red) and gas (blue) matching to WAIS Divide. A negative age
1391 difference implies fewer layers in RICE17 than in WD2014. Blue vertical lines represent 1σ
1392 age uncertainties on Monte Carlo methane matches. The solid red triangle indicates the Pleiades
1393 tephra layer at 165m depth.

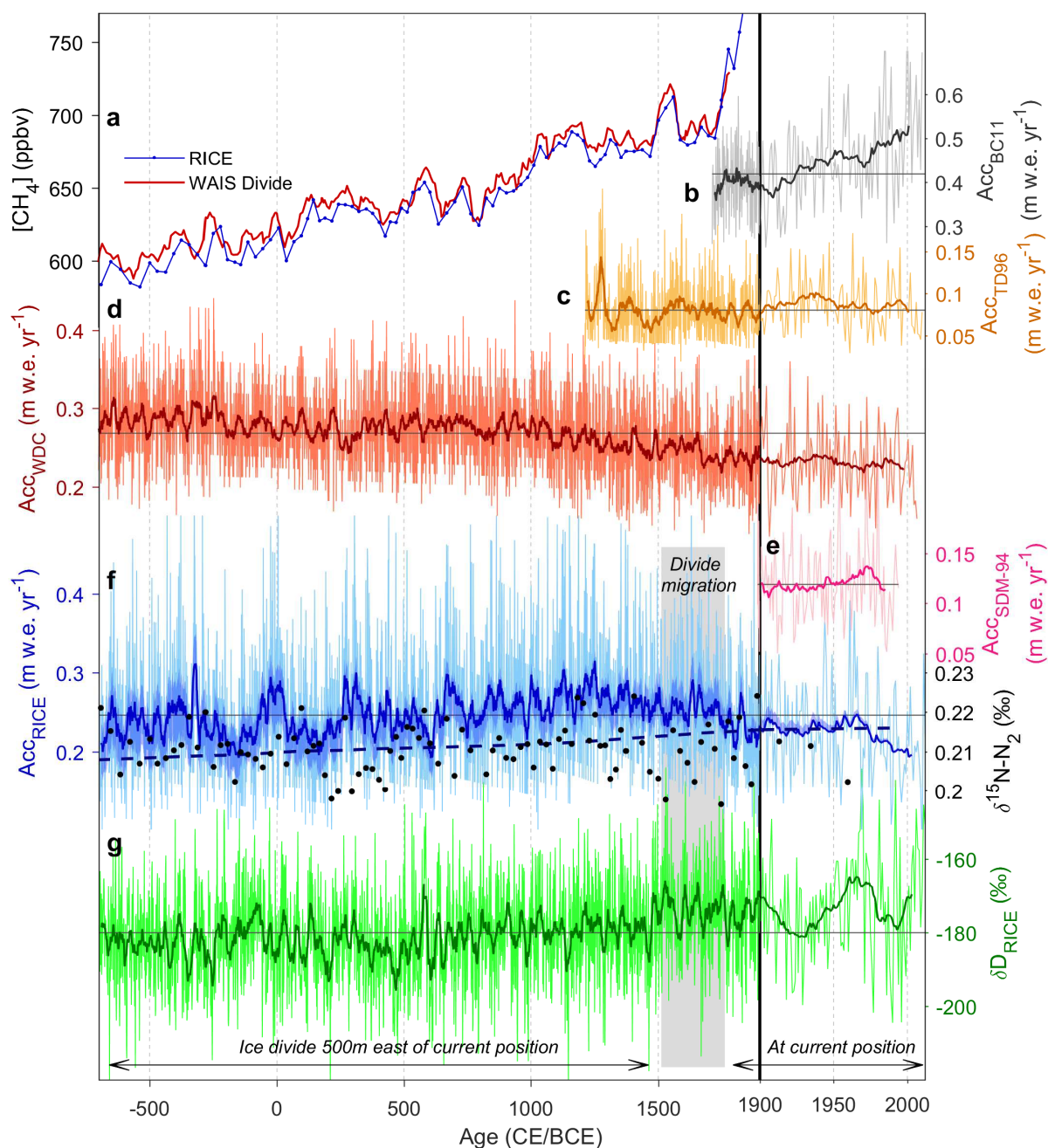


1394

1395 **Figure 10: a)** The RICE volcanic proxy records: non-sea-salt-sulfur (nss-S; orange), ECM
 1396 (purple), acidity (H⁺; red), and non-sea-salt conductivity (nss-cond; blue) based on the
 1397 conductivity-to-calcium (grey, green) excess. Green and blue areas are sections of positive
 1398 excess. **b)** Matching of the RICE records to the WAIS Divide non-sea-salt sulfur record (Sigl
 1399 et al., 2015). Vertical bars indicate volcanic match points (Table 2), with the number of annual
 1400 layers between match points in the two records given according to their respective timescales.
 1401 The red bar represents the Pleiades tephra horizon (1251 CE). Two match points (grey bars)
 1402 had prominent peaks in most records, and an average significance exceeding two standard
 1403 deviations of the general variability of the signal, while the peaks corresponding to two other
 1404 match points (white bars) were less significant. However, direct comparison of calcium and
 1405 conductivity records revealed significant conductivity excess also at these depths.

1406

1407

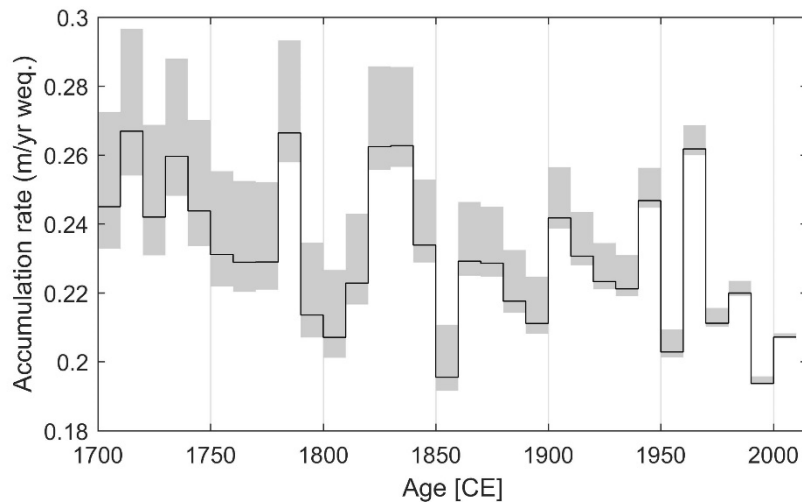


1408

1409 **Figure 11:** **a)** Measured methane concentrations from RICE (blue, on the RICE17 timescale)
 1410 and from WAIS Divide (red, on the WD2014 timescale). **b)** Bryan Coast (BC11, grey),
 1411 Ellsworth Land (Thomas et al., 2015), **c)** Talos Dome (TD96, orange), Northern Victoria Land,
 1412 (Frezzotti et al., 2007; Stenni et al., 2002) (no thinning function applied, extended to 2010 CE
 1413 using stakes measurements), **d)** WAIS Divide (WDC, red), Central West Antarctica (Fudge et
 1414 al. 2016) (corrected for ice advection), **e)** Siple Dome (SDM-94, pink), Marie Byrd Land
 1415 (Kaspari et al. 2004), and **f)** RICE (blue) accumulation histories over the past 2700 years,
 1416 in annual resolution and 20-year smoothed versions (thick lines). The shaded blue area indicates
 1417 the 95% confidence interval of the RICE accumulation rates. The short-lived peak in
 1418 accumulation rates around 320 BCE is likely to be an artefact caused by timescale inaccuracies
 1419 in this period, during which RICE17 diverges from WD2014 (Fig. 9b). Also shown are the gas-

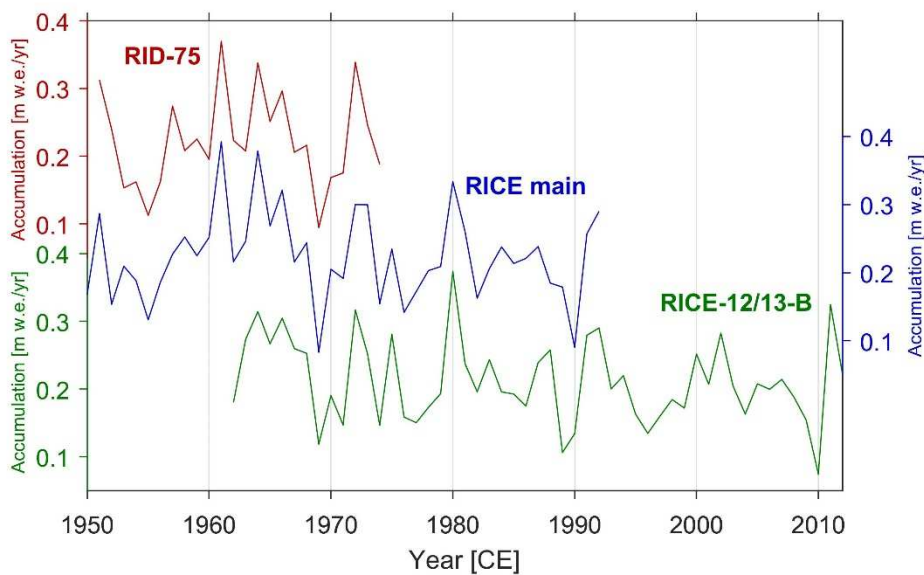
1420 derived accumulation rates for this time interval (f, blue dashed line), and measurements of
 1421 $\delta^{15}\text{N}$ of N_2 informing on past firn column thickness (f, black dots; on the RICE gas timescale).
 1422 **g**) RICE stable water isotope record (δD). Thick green line is a 20-year smoothed version of
 1423 the isotope profile. Grey horizontal lines indicate mean values of the respective accumulation
 1424 rates and δD over the displayed period. Note that the scale changes at 1900 CE (thick vertical
 1425 line). The migration period of the Roosevelt Island ice divide is marked with a grey box.

1426
 1427



1428
 1429 **Figure 12:** Decadal accumulation rates at Roosevelt Island since 1700 CE. Grey shadows
 1430 indicate the 95% uncertainty bounds on the accumulation rate reconstruction due to
 1431 uncertainties in the thinning function.

1432



1433
 1434 **Figure 13:** Accumulation reconstructions since 1950 CE for the three Roosevelt Island ice
 1435 cores described in Table 1.

1436
 1437

1438

1439 **Tables**

Ice core:	RID-75	RICE	RICE-12/13-B
Drilled	1974/75	2011/12 (0-130 m) 2012/13 (130-764.6 m)	Jan 2013
Depth	0-10.68 m	8.57-764.60 m	0-19.41 m
Location	79°22' S, 161°40' W	79°21.839' S, 161°42.387' W	79°21.726' S, 161°42.000' W
Data sets:			
β -activity	16 cm resolution (Clausen et al., 1979)	-	-
$\delta^{18}\text{O}$, δD	Only $\delta^{18}\text{O}$; 4 cm resolution (Clausen et al., 1979)	Continuous and 2 cm resolution (Bertler et al., 2018)	Continuous and 2 cm resolution (Bertler et al., 2018)
CFA	-	H^+ , Ca^{2+} , conductivity, dust, BC; 8.57-344 m; continuous (this work)	H^+ , Ca^{2+} , conductivity, dust, BC; continuous (this work)
ECM	-	49-344 m; continuous (this work)	-
IC	-	Na^+ , Ca^{2+} , Mg^{2+} , SO_4^{2-} ; 8.57-20.6 m; 4 cm resolution (pers. comm., N. Bertler)	Na^+ , Ca^{2+} , Mg^{2+} , SO_4^{2-} ; 4.5 cm resolution (pers. comm., N. Bertler)
ICP-MS	-	S, Na, I; 8.57-249 m; 2-7 cm resolution (pers. comm., P. Mayewski)	S, Na, I; 9.5 cm resolution (pers. comm., P. Mayewski)
	-	Pu^{239} ; 8.64-40m; 4 cm resolution (pers. comm., R. Edwards)	-
CH_4 $\delta^{18}\text{O}_{\text{atm}}$	-	Discrete samples (Lee et al., 2018)	-

1440

1441 **Table 1:** The Roosevelt Island ice and firn core records used in this study.

1442

Depth (m)	RICE17 age (CE)	Significance of volcanic peak (σ)	Event	WD2014 age (CE)
0	2013.0±0	-	Snow surface in RICE-12/13-B (Jan 2013)	-
14.62	1975.1±1	-	Isotope match to RID-75 snow surface (winter 74/75)	-
16.18	1970.9±1	-	Radioactivity peak (winter 1970/71 ¹)	-
18.10-18.20*	(1965.0-1965.2) ±1	-	Tephra likely from Raoul Island, New Zealand (Nov 1964)	(1964.7-1964.9) ±1
21.98	1954.7±1	-	Onset of high radioactivity levels from Castle Bravo, Marshall Islands (March 1954)	-
37.45	1903.8±1	2.7	Santa Maria, Guatemala (Oct 1902)	1904.0±1
42.34	1885.0±1	1.3	Krakatau, Indonesia (Aug 1883), bipolar	1885.0±1
47.90	1863.3±2	>3	Makian, Indonesia (Dec 1861), bipolar	1863.9±1
59.46 [#]	1817.0±4	1.9	Tambora, Indonesia (April 1815), bipolar	1816.4±0
80.09 [#]	1722.3±6	2.0	Unknown	1723.5±1*
85.99	1695.0±6	1.0	Unknown, bipolar	1695.8±1
97.12	1641.2±7	2.0	Parker Peak, Philippines (Jan 1641), bipolar	1642.4±1
105.58 [#]	1599.3±8	2.3	Huaynaputina, Peru (Feb 1600), bipolar	1600.9±1
122.67	1507.0±10	1.9	Unknown	1506.7±2
125.19	1493.4±10	2.8	Unknown	1492.4±2*
131.04	1458.4±10	>3	Kuwae, Vanuatu, bipolar	1459.8±2
145.15	1376.2±11	2.0	Unknown	1378.7±2
161.02	1277.3±12	1.2	Unknown	1277.2±2
162.17	1269.9±13	>3	Unknown	1269.7±2
164.06	1257.3±13	>3	Samalas, Indonesia, bipolar	1258.9±1
165.01-165.02*	1251.5±13	-	Tephra from the Pleiades, West Antarctica	1251.6±2
166.68	1242.3±13	1.0	Unknown	1241.9±2

168.32	1231.4±13	>3	Unknown, bipolar	1230.7±2
174.50	1190.1±14	1.2	Unknown, bipolar	1191.9±2
180.01	1152.3±16	1.9	Unknown	1153.0±2
194.81	1043.3±18	2.9	Unknown	1040.3±2
203.44	974.5±19	2.8	Unknown, bipolar	976.0±2
208.11	937.1±20	1.0	Unknown	939.6±2*
211.02 ^x	912.6±20	2.0	Unknown, bipolar	918.1±2
212.03 ^x	903.9±20	2.6	Unknown	909.0±2*
212.88 ^x	896.3±20	1.9	Unknown, bipolar	900.9±2
222.94	813.2±20	2.3	Unknown, bipolar	819.9±2
232.66	720.3±21	>3	Unknown	726.1±2
235.78	693.1±22	2.0	Unknown, bipolar	698.0±2
236.94	683.0±22	1.7	Unknown, bipolar	685.9±2
237.25	680.1±22	>3	Unknown, bipolar	682.9±2
247.49	575.1±27	2.1	Unknown, bipolar	576.2±2
250.93	539.2±27	1.4	Unknown, bipolar	541.7±3
260.59	434.3±29	>3	Unknown, bipolar	435.4±3
264.19	394.4±30	2.5	Unknown, bipolar	395.5±3
267.41	356.9±30	>3	Unknown, bipolar	360.8±3
276.06	264.3±31	>3	<i>Unknown, bipolar</i>	266.6±3
278.41	236.4±31	1.4	Taupo (New Zealand), bipolar	237.1±3
280.82	205.3±32	2.5	Unknown	207.1±3
283.36 [†]	170.9±33	1.5	Unknown, bipolar	171.0±3
284.97	148.1±34	1.1	Unknown	143.9±3
286.17	131.6±35	2.8	Unknown	125.3±4
286.40	128.1±35	2.8	Unknown	121.9±4
287.49	113.4±35	1.5	Unknown	105.5±4
288.11	105.2±35	2.3	Unknown	97.8±4*
288.35	102.3±35	1.8	Unknown	96.0±4
289.18	90.8±36	2.6	Unknown	83.8±4
289.54	86.2±36	1.4	Unknown	77.5±4*
292.80	41.2±37	2.2	Unknown	31.7±4
296.12 [#]	3.1±37	1.8	Unknown	-7.5±4
297.24 [#]	-10.4±37	2.2	Unknown	-20.3±4

299.30 [#]	-34.0±37	1.8	Unknown	-46.3±4
306.39	-130.9±39	2.3	Unknown	-143.1±4*
306.89	-137.9±39	>3	Unknown	-148.1±4
317.30	-295.9±41	>3	Unknown	-307.2±4*
320.87	-344.4±41	>3	Unknown	-357.0±5
322.15	-362.8±41	1.8	Unknown	-376.5±5
323.14	-376.7±41	2.1	Unknown	-392.1±5
323.84	-385.7±42	1.6	Unknown	-402.7±5*
325.25	-405.7±42	>3	Unknown	-426.1±5*
328.05 [⊗]	-446.6±42	3.1	Unknown	-469.1±5*
331.21	-496.4±43	2.3	Unknown	-519.9±5*
334.94	-554.7±43	>3	Unknown	-581.0±5*
335.84	-567.5±43	>3	Unknown	-596.6±5*
343.30 [#]	-691.5±44	2.7	Unknown	-722.0±6*

1444 1: Age from Clausen et al. (1979). ★Depths indicate the tephra sampling interval. #: CFA acidity is missing for
1445 relevant interval, attribution is based on remaining records. †Significant peak only in nss-conductivity. x:
1446 Conductivity and Ca records missing for interval. ⊗: CFA and IC data missing, depth annotation based on ECM
1447 only. *: Eruption not identified in existing compilation of volcanic eruptions in WAIS Divide (Sigl et al., 2013).

1448 **Table 2:** Marker horizons used for development and validation of the RICE17 chronology.
1449 Strata in bold were used for constraining the timescale. The statistical significance of volcanic
1450 peaks in the RICE records (column 3) is given in terms of the average peak size in smoothed
1451 and standardized versions of the four records (ECM, H⁺, nss-cond, nssS (down to 249m)),
1452 computed relative to a running mean and standard deviation. Volcanic matching to WAIS
1453 Divide allows comparison between RICE17 ages (with 95% confidence interval indicated) and
1454 the corresponding WD2014 ages with associated uncertainties (Sigl et al., 2015, 2016).
1455 Indicated depths and ages correspond to peaks in the volcanic proxies. Below 42.3m, decimal
1456 ages have been calculated assuming BC to peak Jan 1st. Historical eruption ages (column 4)
1457 indicate starting date of the eruption. In column 4 is also stated whether the eruption previously
1458 has been observed to cause a bipolar signal, based on the compilation in Sigl et al. (2013), here
1459 updated to the WD2014 timescale. Since this compilation only identifies bipolar volcanoes back
1460 to 80 CE, volcanoes prior to this are not classified. Three exceptionally large volcanic signals
1461 observed in the RICE core are indicated in italics.

1462

1463

Change point	Time period (rounded)	Mean accumulation rate [m. w.e./yr]	Accumulation rate trend [mm w.e. yr ⁻²]
1287 CE (1291 ± 135)*	700 BCE – 1300 CE	0.25 ± 0.03	+0.02 (0.020 ± 0.003)
1661 CE (1675 ± 123)*	1300 CE – 1650 CE	0.26 ± 0.02	-0.04 (-0.03 ± 0.03)
1966 CE (1969 ± 34)	1650 CE – 1965 CE	0.24 ± 0.01	-0.10 (-0.08 ± 0.05)
	1965 CE – 2012 CE	0.210 ± 0.002	-0.80 (-0.84 ± 0.76)

1464

*Change point not well-determined from bootstrap analysis.

1465 **Table 3:** Mean value and trends in RICE accumulation rates during various time periods.
 1466 Change points and trends are found using break-fit regression (Mudelsee, 2009). The most
 1467 likely change-points and trend values are provided, as well as the associated confidence
 1468 intervals (in parenthesis: median and median absolute deviation) determined from block
 1469 bootstrap analysis. Uncertainties (95% confidence intervals) on mean accumulation rates are
 1470 calculated based on the uncertainty in the accumulation reconstruction. Accumulation trends
 1471 estimates from the bootstrap analysis (in parenthesis) includes uncertainties in determination of
 1472 the change-point, but not uncertainties associated with the derived accumulation rate history.
 1473 The analysis does not account for a potential bias due to ice divide migration, which may
 1474 slightly affect the mean accumulation rate values prior to 1750 CE, and the trend during the
 1475 period of divide migration (~1500-1750 CE).

1476

1477

Rank	Decade	Decadal mean accumulation rate [m. w.e./yr]
1	1990-1999	0.194 ± 0.001
2	1850-1859	0.196 ± 0.010
3	1950-1959	0.203 ± 0.004
4	1800-1809	0.207 ± 0.013
5	2000-2009	0.207 ± 0.001
6	1970-1979	0.211 ± 0.008

1478

1479 **Table 4:** Ranking of decades since 1700 CE according to lowest mean accumulation.
 1480 Uncertainties (95% confidence interval) on the mean values are due to uncertainties in the
 1481 accumulation reconstruction.